Available online at www.sciencedirect.com

ScienceDirect

Geochimica et Cosmochimica Acta 179 (2016) 177–202

Geochimica et Cosmochimica Acta

www.elsevier.com/locate/gca

Experimental investigation of As, Sb and Cs behavior during olivine serpentinization in hydrothermal alkaline systems

Romain Lafay [a,b,*], German Montes-Hernandez [a,c], Emilie Janots [a], Manuel Munoz [a], Anne Line Auzende [a], Antoine Gehin [a], Rodica Chiriac [d], Olivier Proux [e]

[a] Université Grenoble Alpes, ISTerre, F-38041 Grenoble, France
[b] Institute of Earth Sciences, University of Lausanne, CH-1015 Lausanne, Switzerland
[c] CNRS, Institut des Sciences de la Terre (ISTerre), F-38041 Grenoble, France
[d] Université Lyon 1, Laboratoire des Multimatériaux et Interfaces, UMR CNRS 5615, 43 bd du 11 novembre 1918, 69622 Villeurbanne Cedex, France
[e] Observatoire des Sciences de l'Univers de Grenoble, UMS 832 CNRS, Université Joseph Fourier, F-38041 Grenoble Cedex 9, France

Received 4 December 2014; accepted in revised form 10 February 2016; Available online 16 February 2016

Abstract

While Fluid-Mobile Elements (FMEs) such as B, Sb, Li, As or Cs are particularly concentrated in serpentinites, data on FME fluid–serpentine partitioning, distribution, and sequestration mechanisms are missing. In the present experimental study, the behavior of Sb, As and Cs during San Carlos olivine serpentinization was investigated using accurate mineralogical, geochemical, and spectroscopic characterization. Static-batch experiments were conducted at 200 °C, under saturated vapor pressure (≈1.6 MPa), for initial olivine grain sizes of <30 μm (As), 30–56 μm (As, Cs, Sb) and 56–150 μm (Cs) and for periods comprised between 3 and 90 days. High-hydroxyl-alkaline fluid enriched with 200 mg L^{-1} of a single FME was used and a fluid/solid weight ratio of 15. For these particular conditions, olivine is favorably replaced by a mixture of chrysotile, polygonal serpentine and brucite. Arsenic, Cs or Sb reaction product content was determined as a function of reaction advancement for the different initial olivine grain sizes investigated. The results confirm that serpentinization products have a high FME uptake capacity with the partitioning coefficient increasing such as $^{Cs}D_{p/fl} = 1.5–1.6 < {}^{As}D_{p/fl} = 3.5–4.5 < {}^{Sb}D_{p/fl} = 28$ after complete reaction of the 30–56 μm grain-sized olivine. The sequestration pathways of the three elements are however substantially different. While the As partition coefficient remains constant throughout the serpentinization reaction, the Cs partition coefficient decreases abruptly in the first stages of the reaction to reach a constant value after the reaction is 40–60% complete. Both As and Cs partitioning appear to decrease with increasing initial olivine grain size, but there is no significant difference in the partitioning coefficient between the 30–56 and 56–150 μm grain size after complete serpentinization. X-ray absorption spectroscopy (XAS) measurements combined with X-ray chemical measurements reveal that the As(V) is mainly adsorbed onto the serpentinization products, especially brucite. In contrast, mineralogical characterization combined with XAS spectroscopy reveal redox sensitivity for Sb sequestration within serpentine products, depending on the progress of the reaction. When serpentinization is <50%, initial Sb(III) is oxidized into Sb(V) and substantially adsorbed onto serpentine. For higher degrees of reaction, a decrease in Sb sequestration by serpentine products is observed and is attributed to a reduction of Sb(V) into Sb(III). This stage is characterized by the precipitation of Sb–Ni-rich phases and a lower bulk partitioning coefficient compared to that of the serpentine and brucite assemblage. Antimony reduction appears linked to water reduction accompanying the bulk iron oxidation, as half the initial Fe(II) is oxidized into Fe(III) and incorporated into the serpentine products

* Corresponding author at: Institute of Earth Sciences, University of Lausanne, CH-1015 Lausanne, Switzerland.
E-mail address: romain.lafay@unil.ch (R. Lafay).

http://dx.doi.org/10.1016/j.gca.2016.02.014

once the reaction is over. The reduction of Sb implies a decrease of its solubility, but the type of secondary Sb-rich phases identified here might not be representative of natural systems where Sb concentrations are lower. These results bring new insights into the uptake of FME by sorption on serpentine products that may form in hydrothermal environments at low temperatures. FME sequestration here appears to be sensitive to various physicochemical parameters and more particularly to redox conditions that appear to play a preponderant role in the concentrations and mechanism of sequestration of redox-sensitive elements.

1. INTRODUCTION

Serpentine minerals are ubiquitous in ultramafic rock alteration, or "serpentinization", at temperatures below 400 °C. This hydrothermal alteration reaction leads to the hydration of the upper mantle, especially at slow spreading ridges, and to the formation of serpentinite rock, which constitute up to 15% of the ocean floor lithosphere (Carlson, 2001; Mével, 2003). In the last decade, the number of studies investigating the trace element geochemistry of ocean floor serpentinites has considerably increased (Paulick et al., 2006; Agranier et al., 2007; Vils et al., 2009; Pabst et al., 2011; Kodolányi et al., 2012). Serpentinites are assumed to control much of the transfer of water and trace elements from the hydrated oceanic lithosphere (Bonatti et al., 1984; Vils et al., 2008) to the subduction environment (Rüpke et al., 2004; Hattori and Guillot, 2007; Deschamps et al., 2011,2012; Kodolanyi and Pettke, 2011; Kodolányi et al., 2012). Serpentinites from the oceanic lithosphere are characterized by high enrichment in FME (B, Sb, As, Li Cs, Pb, and Cl) with respect to primary minerals from peridotite (olivine and pyroxenes; Hattori and Guillot, 2003; Paulick et al., 2006; Agranier et al., 2007; Lee et al., 2008). In the abyssal environment, FME enrichment in serpentinites is explained by the intense hydrothermal activity under very high fluid/rock ratios (Schmidt et al., 2007; Delacour et al., 2008a,b; Rouméjon and Cannat, 2014). The enrichment is not surprising in the case of elements such as Cl and to a lesser extent B that are abundant in seawater. However, the enrichment in As, Sb and Cs is more complex to explain and certainly invoke the combination of several parameters (FME source, pH, T, fluid/rock ratio) to account for their large concentration ranges (up to hundreds of $\mu g\ g^{-1}$) measured in natural serpentinites (Deschamps et al., 2013 and reference therein).

With increasing P–T conditions towards the subduction zone, FME trapped by serpentine are remobilized by desorption or structural removal (Philippot et al., 2007; Vils et al., 2011; Lafay et al., 2013) accompanying serpentine phase transformation (e.g. lizardite to antigorite), and dehydroxylation (Scambelluri and Philippot, 2001; Scambelluri et al., 2004a,b; Vils et al., 2011). Water released from the subducted lithosphere during serpentine breakdown into olivine (Schmidt and Poli, 1998; van Keken et al., 2011) can induce partial melting within the overlying mantle wedge, leading to arc magmatism with a specific FME signature (Kerrick, 2002; Tatsumi, 2005) depending on the FME discharge depth (Hattori and Guillot, 2003; Scambelluri et al., 2004a,b; Deschamps et al., 2013). Therefore, FME are considered to be powerful geochemical tracers of the slab (including sediments) dehydration in the subduction zone (Scambelluri et al., 2004a,b; Savov et al., 2005; Hattori and Guillot, 2007; Deschamps et al., 2011,2012, 2013).

FME sequestration processes and partitioning by serpentinite minerals during peridotite alteration are little understood. It is of prime importance to investigate the distribution and sequestration mechanism of FME during serpentine formation from hydrothermal alteration of olivine, since they control the FME mobility in response to fluid circulation or recrystallization/dehydration reactions occurring to the oceanic lithosphere in abyssal and subduction environments. In natural serpentinites, determining the FME distribution is challenging due to the low FME concentration and the microscopic crystal size of serpentinite minerals. While a large number of high quality bulk serpentinite rock compositions is available (e.g. Hattori and Guillot, 2007; Kodolányi et al., 2012), the lack of spatial control of this method hampered the characterization of FME distribution in the serpentinite minerals (e.g. serpentine, brucite, magnetite, talc and other accessory minerals). Although laser ablation coupled ICP-MS and NanoSIMS investigations (e.g. Deschamps et al., 2010, 2011; Pabst et al., 2011; Kodolányi et al., 2012) record in-situ high-precision analyses on serpentinites, the analytical volumes are still commonly higher than the crystal size of single serpentinite minerals. Therefore, data interpretation in order to determine trace element distribution is restricted mainly by the limit of detection (spatial and concentration) and the difficulty in determining FME sequestration processes. Indeed, not only the FME distribution but also the sequestration mechanisms need to be characterized in order to determine if FME adsorbed on the mineral surface or incorporated in the crystal lattice of serpentine (Wunder et al., 2010).

Hydrothermal experiments have been used successfully to investigate the reaction processes of peridotite serpentinization (e.g. kinetics, cracking propagation or potential H_2 production) and influence of the overriding parameters (temperature, pressure, pH) (Seyfried and Dibble, 1980; Macleod et al., 1994; James et al., 2003; Seyfried et al., 2007; McCollom and Bach, 2009; Hövelmann et al., 2011). Nevertheless only a few experimental studies have focused on FME partitioning during serpentinization processes (Wunder et al., 2010; Lafay et al., 2014). In this study, a series of San Carlos olivine hydrothermal alteration experiments was conducted to investigate the behavior and sequestration of As, Sb and Cs during

serpentinization under high pH fluid conditions at 200 °C. Such alkaline conditions were chosen because they show the fastest serpentinization kinetics with well-characterized alteration products represented by the association of chrysotile and brucite (Lafay et al., 2012). Alkaline conditions are also representative of some hydrothermal fields in which high pH fluids are observed, such as the famous Lost City (Ludwig et al., 2006; Foustoukos et al., 2008). The main goals of this study are to (1) determine the FME distribution and the sequestration mechanism in the reaction products, (2) evaluate the influence of the extensive parameters (e.g. grain size, serpentinization extent) on the FME partitioning mechanisms, and (3) provide an estimation of FME partitioning between fluid and solid ($^{FME}D_{p/fl}$), during serpentinization. For these purposes, we rely on accurate mineral product characterization using conventional-resolution (e.g. electron probe microanalyses (EPMA), thermogravimetric analyses (TGA)) and high-resolution tools such as transmission electron microscopy (TEM), Mössbauer spectroscopy or (XAS) at the As and Sb K-edges to determine the speciation and coordination of As and Sb in the reaction products. This highly comprehensive approach required overcoming FME concentration detection limit in solid products (typically few 100's to 1000's $\mu g\ g^{-1}$ for EPMA and XAS), which explains for the 200 $mg\ L^{-1}$ FME concentration used in the starting experimental fluid (Lafay et al., 2014).

2. EXPERIMENTS AND ANALYTICAL TECHNIQUES

2.1. Experimental procedure

Experiments concerning olivine mineral serpentinization under hydrothermal conditions were conducted in small static batches in a Teflon-lined cell. Experiments were performed using 1.5 ml of high alkaline solution (1 M of NaOH, pH ≈ 13.5 at 25 °C) reacting with 100 mg of San Carlos olivine at 200 °C under constant saturated pressure (~16 bar). The high fluid–rock ratio (~15) favored fast reaction kinetics controlled by the initial olivine grain size. The starting solution was systematically doped with dissolved As, Sb or Cs at a concentration of 200 $mg\ L^{-1}$. The respective sources of As(V), Sb(III) and Cs(I) were $Na_2HasO_4{\cdot}7(H_2O)$, $SbCl_3$ and $CsNO_3$. The relatively high FME concentrations in the starting fluid may have only minor impact on the sequestration mechanism and fluid/-solid distribution coefficient in comparison to lower concentrations typical of those encountered in natural environments (Lafay et al., 2014).

Three different grain sizes were used as starting materials: <30 μm; 30–56 and 56–150 μm in order to investigate FME partitioning for different specific olivine surface areas and therefore different durations and kinetic regimes. Based on previous results obtained in undoped solutions (Lafay et al., 2012), the experiments were left to run for 3–35 days for <30 μm sized grains and for 3–90 days for 30–56 and 56–150 μm size grains in order to cover almost the complete serpentinization reaction. A summary of the hydrothermal experiments performed is provided in Table 1.

At the end of each experiment, the autoclave was dipped in cold water to quench it quickly and avoid possible subsequent dissolution/precipitation reactions of the serpentinization product. The fluid was then collected and filtered through a 0.22 μm pore-size filter and the pH was measured to ensure that there was no substantial change (note that the pH remains constant and close to 10.1 at 200 °C during the entire experiment, 13.5 at 25 °C). The solid product was washed several times and dried directly in the Teflon cell at 80 °C for 24 h and recovered for the further physicochemical characterizations described below. Quenching avoids significant perturbation of the solid reaction products, but may modify the chemistry of the recovered fluids (as shown by modeling, Fritz et al., 2013) as a result of cooling and depressurization processes causing low-temperature precipitation of the salts. Indeed, composition of recovered fluids might not reflect composition at equilibrium. For these reasons, interpretations of FME partitioning between fluid and solid, distribution and sequestration mechanism are based on characterization of the washed solid products assumed to be representative of the alteration reaction under the given experimental conditions.

2.2. Analytical techniques

2.2.1. X-ray powder diffraction (XRD)

X-ray powder diffraction (XRD) analyses were performed in order to identify the minerals at the end of each experiment. All the samples were crushed manually in an agate mortar. The powders were carefully loaded and manually compacted in borosilicated capillaries 500 μm in diameter, which corresponds to about 5 mg of sample. XRD patterns were recorded with a Bruker D8 powder diffractometer equipped with a SolX Si (Li) solid state detector from Baltic Scientific Instruments using CuKα1–Kα2 radiation and a Göbel mirror. Intensities were recorded for a 2θ interval from 5° to 80° with an 8 s counting time per n.d.24° 2θ step for bulk mineralogy determination.

2.2.2. Fourier transform infrared spectroscopy (FTIR)

FTIR measurements were performed using a Bruker Hyperion 3000 IR microscope. The IR beam was focused through a 15× lens and the typical size of the infrared aperture was 50 × 50 μm^2. The light source was a GlobarI and the beam splitter was in KBr. The spectra were measured from 700 to 4000 cm^{-1} (4 cm^{-1} resolution) with a MCT monodetector cooled by liquid nitrogen. Sample preparation involved careful crushing in a mortar and manual compaction of the fine crushed particles between two KBr windows to obtain a thickness <100 μm. Five spectra were obtained per sample and we used OPUS software to fit the results and compare the spectra from the experimental products.

2.2.3. Field emission gun scanning electron microscopy (FESEM) and transmission electron microscopy (TEM)

Imaging of experimental products was done using secondary or backscattered electron detection modes to evaluate the mineral sizes and morphologies. Micro-imaging was

Table 1
Summary of the results from hydrothermal alteration of olivine. Mineral modal compositions were calculated from TG measurements and Cs, Sb and As concentration in experimental solid phases were determined by ICP-MS.

Sample	Olivine Grain size	Reaction time	Mineral content (mass%)			Reaction advancement	Bulk rock FME content (μg g^{-1})			FME concentration in residual fluid (mg L^{-1})	FME concentration in reaction product (μg g^{-1})	($^{FME}D_{s/fl}$)	($^{FME}D_{p/fl}$)
	(μm)	(days)	Olivine	Brucite	Chrysotile	(%)	Cs	Sb	As			[bulk]/[fluid]	[product]/[fluid]
Cs-1	30–56	3	80	1	19	20	192	–	–	187	960	1.0	5.1 ± 0.3
Cs-2	30–56	10	68	2	30	32	235	–	–	184	734	1.3	4 ± 0.2
Cs-3	30–56	24	46	4	50	54	275	–	–	182	509	1.5	2.8 ± 0.2
Cs-4	30–56	50	32	5	62	67	193	–	–	187	288	1.0	1.5 ± 0.1
Cs-5	30–56	90	0	7	93	100	289	–	–	181	289	1.6	1.6 ± 0.1
Cs-5 dup	30–56	90	0	7	93	100	269	–	–	182	269	1.5	1.5 ± 0.1
Cs-6	56–150	13	88	2	10	12	108	–	–	193	900	0.6	4.7 ± 0.3
Cs-7	56–150	32	71	2	26	28	130	–	–	191	464	0.7	2.4 ± 0.1
Cs-8	56–150	60	53	3	45	48	163	–	–	189	340	0.9	1.8 ± 0.1
Cs-9	56–150	90	41	3	53	56	181	–	–	188	323	1.0	1.7 ± 0.1
Sb-1	30–56	3	86	1	13	14	–	529	–	165	3779	3.2	22.9 ± 1.3
Sb-2	30–56	10	80	1	19	20	–	775	–	148	3875	5.2	26.1 ± 1.5
Sb-3	30–56	25	53	3	44	47	–	2015	–	66	4287	30.7	65.3 ± 3.8
Sb-4	30–56	50	15	7	78	85	–	1953	–	70	2298	28.0	32.9 ± 1.9
Sb-5	30–56	90	5	7	88	95	–	1919	–	72	2020	26.6	28 ± 1.5
As-1	<30	3	54	4	42	46	–	–	510	166	1109	3.1	6.7 ± 0.4
As-2	<30	13	17	6	77	83	–	–	1016	132	1224	7.7	9.3 ± 0.6
As-3	<30	20	11	6	84	90	–	–	971	135	1079	7.2	8 ± 0.5
As-4	<30	35	0	8	92	100	–	–	1091	127	1091	8.6	8.6 ± 0.6
As-5	30–56	3	80	1	19	20	–	–	177	188	885	0.9	4.7 ± 0.3
As-6	30–56	10	68	2	30	32	–	–	101	193	316	0.5	1.6 ± 0.1
As-7	30–56	24	50	4	46	50	–	–	381	175	762	2.2	4.4 ± 0.3
As-8	30–56	41	17	6	76	82	–	–	491	167	599	2.9	3.6 ± 0.2
As-9	30–56	51	24	5	72	77	–	–	448	170	582	2.6	3.4 ± 0.2
As-10	30–56	72	5	7	89	96	–	–	551	163	574	3.4	3.5 ± 0.2
As-11	30–56	90	0	8	92	100	–	–	610	159	610	3.8	3.8 ± 0.2

[β]Mineral modal proportion were calculated from TG measurements and the estimated error is below 2 wt.% for brucite and below 5 wt.% for serpentine.
[γ]Concentration in equilibrium fluid were calculated by mass balance in relative weight percent.
[δ]Solid/fluid FME distribution coefficients between bulk solid and fluid $^{FME}D_{s/fl}$ and between alteration product and fluid $^{FME}D_{p/fl}$ were determined from Bulk ICP-MS measurements and TGA analyses.

done using Zeiss Ultra 55 Field emission gun scanning electron microscopy (FESEM) to obtain a spatial resolution of approximately 1 nm at 15 kV. The samples were dispersed by ultrasonic treatment in absolute ethanol for at least 5 min in order to disaggregate the particles. One or two drops of dispersion were placed on an aluminum support and coated with a thin film of platinum for SEM observation.

Additionally, a drop of the chrysotile suspension in ethanol was deposited on to perforated carbon foil supported on conventional copper micro-grids for further observations with a JEOL 2100F transmission electron microscope (TEM) operating at 200 kV, equipped with a field emission gun and a high-resolution pole piece achieving a point-to-point resolution of 1.8 Å.

2.2.4. Thermogravimetric analyses (TGA)

TGA for experimental solid products were performed with a TGA/SDTA 851^e Mettler Toledo instrument under the following conditions: sample mass of about 10 mg, 150 µl platinum crucible with a pinhole, heating rate of 10 °C min^{-1}, and inert N_2 atmosphere of 50 ml min^{-1}. The sample mass loss and associated thermal effects were obtained by TGA/DTGA in a temperature range from 30 to 1200 °C. This method allowed us to determine the proportion of each phase by using the TGA first derivative (rate of mass loss: Lafay et al., 2012). The TGA apparatus was calibrated in terms of mass and temperature. Calcium oxalate was used to calibrate the mass of the sample. The melting points of three compounds (indium, aluminum and copper) obtained from the DTGA signals were used to calibrate the temperature of the sample. The temperature accuracy of the TGA/SDTA system is about ±0.25 °C. The weighting accuracy is around 0.1 µg, which corresponds to 0.01% for a 10 mg sample. Due to the possible changes and shifts in the dehydroxylation range of serpentinization products in the course of the experiments, we estimate that the uncertainties with regard to the estimation of phase proportions are below 5 wt.%.

2.2.5. Inductively coupled plasma mass spectrometry (ICP-MS)

Arsenic, Sb and Cs concentrations were determined by Inductively Coupled Plasma Mass Spectrometry (ICP-MS) using an Agilent 7500ce at the ISTerre laboratory. About 10 mg of sampled Sb, As and Cs was crushed in an agate ring mill before acid digestion by HF and HNO_3. The complete analytical procedure is described in (Chauvel et al., 2011). The precision and accuracy were assessed by repeated ICP-MS analyses of three rock standards: serpentinite UBN, basalts BR-24 and BCR-2. Our results show good agreement between measured and certified values for these international reference materials (Govindaraju, 1994; Jochum et al., 2005). To assess the accuracy of the elements of interest, we prepared three artificial standards with trace element (Cs, Sb, As) concentrations of respectively 50 10 ng g^{-1} and 0.1 µg g^{-1} in a matrix of 1 µg g^{-1} of Si and Mg. Linear regression obtained on these three artificial standards was used to calculate the concentration in FME-rich experiments separately. Standard deviations were in the following ranges: 0.2–1.5% for As and from 0.2% to 1.2% for Sb and Cs. The limits of detection are ~50 ppb for Sb and Cs and ~200 ppb for As. The concentrations of trace elements in the equilibrium fluids [(aq)] were deduced from the concentrations of trace elements in the starting fluids and the final mineral product concentration [(ctl)] was measured by the method described here.

2.2.6. Electron microprobe (EMP)

Major and FME brucite, serpentine and residual olivine concentrations were determined quantitatively and qualitatively using Electron Microprobe (EMP) analyses and X-Ray mapping. Measurements were performed at the ISTerre laboratory using a JEOL JXA-8230. Serpentinized olivine products were mounted in epoxy studs under vacuum and polished to a quarter micron diamond finish for microprobe analyses. The distribution of the major and trace elements (As, Cs and Sb) was characterized through semi-quantitative X-ray mapping of the serpentinized products obtained for different reaction durations. Mapping for low reaction progress were not possible due to the small size of serpentinized domains. X-ray mapping was done using an accelerating voltage of 15 kV, with a focused beam and a beam current of 12 nA. The combined WDS/EDS method was applied with a mapping size resolution typically around 0.5 µm and 600 ms of counting time per pixel. Quantitative measurements were performed using a WDS detector, an accelerating voltage of 20 kV and a beam current of 50 nA, to evaluate the concentration of As and Sb in the serpentinized product and residual olivine using a spot size of 1 µm and San Carlos olivine as internal standard. The error was lower than 0.3% for Mg and Si, below 0.5% for Fe, and below 2% for Ni, Mn and Na. For the trace elements the error was lower than 13% and comprised between 0.3% and 8% for concentrations higher than 500 ppm. A non-acceptable error and detection limit prevented Cs semi-quantitative measurements. The results from quantitative measurements are reported in Tables 2 and 3 for Sb-rich experiments and As-rich experiments respectively.

2.2.7. Mössbauer measurements

To evaluate the oxidation state of iron in our samples, ^{57}Fe Mössbauer spectrometry was performed at the "Laboratoire de Physique de l'Etat Condensé", of Le Mans University. Fresh olivine was analyzed first. We then analyzed the solid product obtained after a complete alteration experiment starting with 30–56 µm olivine grains. The Mössbauer spectra were recorded at 77 K using a constant acceleration spectrometer and a ^{57}Co source diffusing into a rhodium matrix. Two fitting models refined using a least-squares fitting procedure were considered to describe the Mössbauer spectra and untangle the Fe isomeric shift δ (mm s^{-1}) and the quadrupole splitting Δ (mm s^{-1}) to determine the Fe oxidation state and coordination number.

2.2.8. X-ray absorption fine structure (XAFS) spectroscopy

The XAFS spectra – including the X-ray Absorption Near-edge Structure (XANES) region, and Extended

Table 2
Summary of quantitative electron microprobe oxide composition for experimental product from run Sb-5, after 90 days of reaction at 200 °C and calculated concentration for Sb. n.d. (not detected).

Mineral	Oxide composition (wt.%)								Sb
	MgO	Na_2O	MnO	FeO	NiO	Sb_2O_3	SiO_2	Total	($\mu g\ g^{-1}$)
Olivine	51.8	0.004	0.147	9.0	0.374	0.009	40.5	101.9	75
Olivine	49.3	0.055	0.182	10.2	0.350	0	38.8	99.0	n.d.
Olivine	52.5	0.251	0.191	9.7	0.389	0	39.2	102.4	n.d.
Olivine	47.8	0.016	0.185	10.2	0.341	0	41.7	100.3	n.d.
Olivine	48.3	0.012	0.152	8.9	0.353	0.006	40.6	98.5	50
Olivine	49.0	0.018	0.168	10.3	0.351	0.007	40.8	100.8	58
Olivine	47.6	0.003	0.133	8.8	0.360	0	41.5	98.4	n.d.
Olivine	46.4	0.016	0.132	8.7	0.350	0	38.6	94.3	n.d.
Olivine	50.8	0.020	0.128	8.4	0.367	0	43.8	103.6	n.d.
Serpentine	43.9	0.9	0.2	9.1	0.3	0.2	32.5	87.2	1 646
Serpentine	42.3	1.0	0.13	8.0	0.2	0.19	35.6	87.4	1 612
Serpentine	43.3	1.1	0.14	8.7	0.3	0.3	33.2	87.1	2 539
Serpentine	36.9	1.2	0.09	7.7	0.4	0.5	37.8	84.7	4 219
Serpentine	38.9	1.1	0.08	6.9	0.3	0.27	38.7	86.4	2 214
Serpentine	41.6	0.9	0.1	8.7	0.3	0.33	36.0	88.1	2 782
Serpentine	39.5	1.0	0.09	8.5	0.5	0.41	38.4	88.5	3 458
Serpentine	38.3	2.3	0.08	6.3	0.3	1.0	33.8	82.8	8 404
Serpentine	38.2	1.4	0.1	8.6	0.2	0.26	36.1	85.0	2 130
Serpentine	36.4	1.1	0.07	6.6	0.2	0.36	37.6	82.3	2 957
Serpentine	37.9	0.978	0.133	11.1	0.485	0.008	35.9	86.6	67
Serpentine/brucite	53.6	0.085	0.66	23.7	0.292	0.039	8.4	87.1	326
Serpentine/brucite	46.7	0.3	0.6	16.7	0.084	0.035	13.8	78.2	292
Serpentine/brucite	55.7	0.2	1.1	22.9	0.334	0.032	4.8	85.3	267
Brucite	56.1	0.5	0.6	20.8	0.206	0.024	12.9	91.4	200
Brucite	71.7	0.2	0.7	14.7	0.603	0.006	5.3	93.3	n.d.
Brucite	65.9	0.1	0.8	23.5	0.416	0	4.7	95.6	n.d.
Brucite	63.7	0.1	0.9	19.8	0.355	0	3.8	88.8	n.d.
									($mg\ g^{-1}$)
Accessory phase	33.6	1.1	0.1	10.1	5.7	52.2	18.7	121.5	436
Accessory phase	39.9	1.3	0.0	8.6	5.7	40.1	29.1	124.8	335
Accessory phase	28.8	0.8	0.0	8.9	6.6	46.6	25.2	117.0	390

X-ray Absorption Fine Structure (EXAFS) region – of the experimental solid product were collected in both transmission and fluorescence modes at the As and Sb K-edges on the BM30B-FAME beam line of the European Synchrotron Radiation Facility (ESRF, Grenoble, France; see Proux et al., 2005 for a detailed description of the experimental set-up). A Si (2 2 0) double crystal monochromator was used to select the incident energy. Fluorescence was detected using a Cambera 30-element energy-resolved detector. The intensity of the incident beam was measured using an ion chamber filled with He gas. The beam size on the sample was 300 × 200 μm and each XAS spectrum is an average of 4–6 step-by-step acquisitions with a 0.3 eV energy step and 4 s dwell time. Data normalization (i.e., edge-jump and slope correction), background removal and linear combination fits were performed using the Athena software (Ravel and Newville, 2005).

The samples were carefully diluted in a boron nitride (BN) matrix and XAFS measurements were carried out on sample pellets (1 mm thickness and 5 mm diameter) using a dedicated sample holder. The samples were positioned at 45° in order to optimize the fluorescence on the detector. The sample holder was placed in a helium cryostat at 20 K. Metallic Sb^0 and As^0, Sb_2O_3 and As_2O_3 oxides and both reactants were analyzed as standards.

3. RESULTS

3.1. Reaction mechanism and kinetics

3.1.1. Mineral nature and composition of the experimental solid products

Experimental hydrothermal alteration systematically causes olivine mineral to be replaced by a porous assemblage of fibrous serpentine and idiomorphic brucite with the external shape of the olivine grains being coarsely preserved (Figs. 1 and 2) despite the non-isovolumetric reaction. X-ray diffraction measurements only show the presence of serpentine, brucite and residual olivine (depending on the progress of the reaction) in all the experiments (e.g. Fig. 3a and b). Infrared spectra after complete olivine replacement systematically indicate the presence of chrysotile as the dominant serpentine polymorph for the three classes of grain size used (e.g. Fig. 3c and d). Furthermore,

Table 3
Summary of quantitative electron microprobe oxide composition for experimental product from run As-10, after 90 days of reaction at 200 °C and calculated concentration for As. n.d. (not detected).

Mineral	Oxide composition (wt.%)								As
	MgO	Na_2O	MnO	FeO	NiO	SiO_2	As_2O_5	Total	(μg g^{-1})
Olivine	47.4	0.08	0.018	8.8	0.1	39.2	0	96.0	n.d.
Olivine	49.6	0.07	0.003	8.3	0.1	41.7	0	100.2	n.d.
Olivine	45.8	0.195	0.146	8.5	0.38	37.6	0.01	92.7	78
Olivine	49.4	0.215	0.163	8.6	0.3	40.4	0	99.1	n.d.
Brucite	62.6	0.6	0.9	17.1	0.3	1.9	0.47	84.1	3077
Brucite	61.3	0.9	0.8	15.5	0.2	6.0	0.23	85.1	1473
Brucite	53.4	0.1	0.6	18.9	0.4	7.1	0.42	81.2	2758
Serpentine/brucite	51.7	1.3	0.5	9.8	0.2	15.0	0.13	78.7	861
Serpentine	34.5	1.6	0.1	6.9	0.2	36.2	0.05	79.6	293
Serpentine	34.8	1.5	0.1	6.7	0.3	32.9	0.09	76.4	600
Serpentine	30.7	1.3	0.1	6.3	0.3	33.9	0.05	72.7	346
Serpentine	46.9	1.5	0.1	6.4	0.3	37.2	0.17	92.6	1095
									(mg g^{-1})
Accessory phase	27.2	1.2	0.0	5.0	11.5	29.4	7.9	82.3	51.3
Accessory phase	36.4	1.4	0.1	6.4	1.8	35.7	1.2	83.0	7.8
Accessory phase	35.8	1.5	0.0	4.4	0.6	32.8	0.8	76.0	5.5
Accessory phase	41.6	1.3	0.0	7.5	1.1	30.9	7.8	90.3	50.9

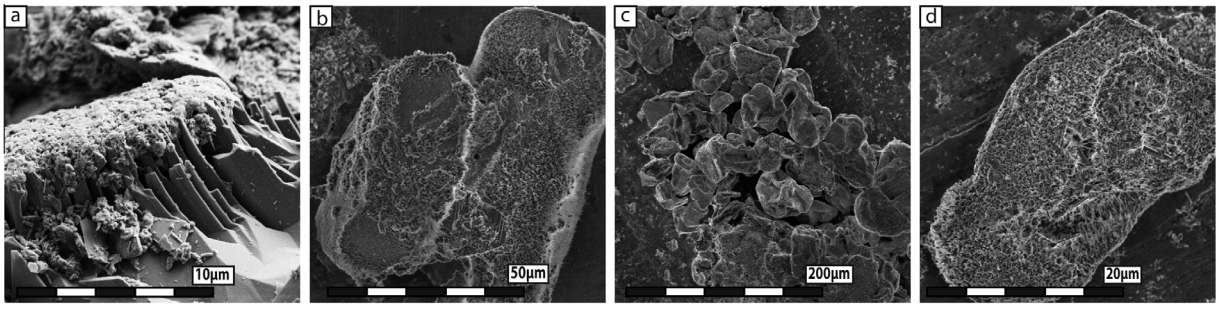

Fig. 1. Scanning electron microscope imaging of the experimental products. All experiments shown were performed at pH 13.5 (at 25 °C) and 200 °C, for 56–150 μm (a) and 30–56 μm (b–d) initial olivine grain sizes, (a) notches after 32 days of reaction in presence of Cs (run Cs-7), (b) olivine grains after 3 days of reaction in presence of Sb (run Sb-1), (c and d) olivine grains after 10 and 72 days of reaction in presence of As (run As-6 and As-10).

chrysotile particles growing from larger initial grain sizes (30–56 and 56–150 μm) are systematically wider. Whatever the initial grain size, occurrence of large particles with a diameter of more than 100 nm, corresponding to 15-sectored polygonal serpentine (Fig. 4), was observed in the case of the longest reaction times (i.e. long-duration serpentinization) (Fig. 2c). This concurs with the results of infrared spectroscopy for advanced reactions (i.e. >50% of mineral replacements) where the Si–O–Si vibration bands (in the 800–1100 cm^{-1} range) are shifted to lower wave numbers for the three peak characteristics of chrysotile (960, 1020 and 1060 cm^{-1}). Indeed, this is a direct consequence of larger chrysotile particle sizes and a mixing between chrysotile and polygonal serpentine. SEM observations and EMP mapping support the precipitation of serpentine and brucite forming a porous medium around the olivine grains (Fig. 5). The replacement fronts commonly appear ruffled, including etch pits and micrometric notches that penetrate further into the olivine following similar orientations (Fig. 5b). The length of the notches varies and they are less than 2 μm in width, which is typical in the case of olivine alteration under hydrothermal conditions (Hövelmann et al., 2011). Pristine olivine grain shapes are mostly preserved (Figs. 1, 2a and 5) but mixing of scattered serpentine and brucite is also observed among serpentinized grains (Fig. 5c). Serpentine assemblages localized at past olivine grain borders are occasionally characterized by apparently larger amounts of iron, producing lighter borders on backscattered electron images, whereas serpentinized olivine cores are characterized by a darker porous medium and lower apparent iron content (Fig. 5d). Grain cores occasionally display voids, suggesting the chemical (dissolution) or mechanical removal of primary or secondary material.

3.1.2. Reaction progress

The amounts of serpentine and brucite (serpentinization degree) were estimated by TGA measurements for each

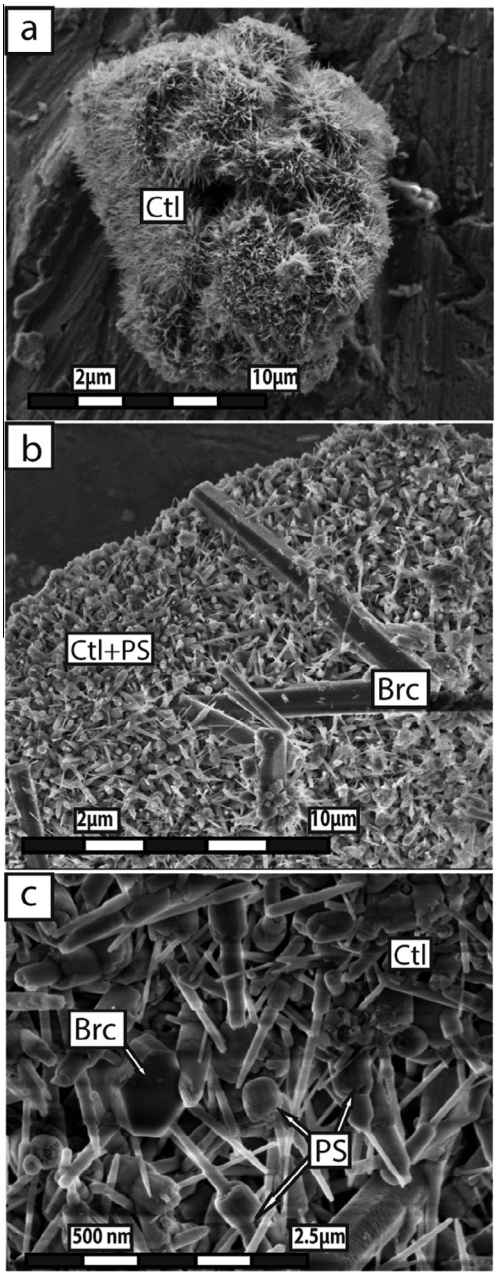

Fig. 2. Scanning electron microscope imaging of the reaction product from olivine alteration, (a) (<30 µm) after 30 days in presence of As-rich solution (run As-4), (b) (30–56 µm) after 90 days in presence of Sb-rich solution (run Sb-5), (c) (56–150 µm) after 90 days in presence of Cs-rich solution (run Cs-9). Ctl: chrysotile, Brc: brucite, PS: polygonal serpentine.

experiment (the results are reported Table 1). This estimation is based on H_2O loss of 13 and 30 wt.% for pure serpentine and brucite respectively in the range 200–1000 °C, assuming that H_2O loss is proportional to the serpentine and brucite phase contents. The complete procedure was described in detail in Lafay et al. (2012).

Thermogravimetric patterns display limited (below 2%) weight loss below 300 °C, which is attributed to molecular water desorption. Brucite dehydroxylation is prompt and occurs between 300 and 400 °C. Serpentine dehydroxylation is characterized by a marked weight loss between 400 and 700 °C. In this range, the features of the TG/DTG curves evolve as a function of reaction advancement (Fig. 6); this indicates a substantial change in the properties of the serpentine phase throughout the experiments, regardless of the grain size in question. DTG serpentine patterns are characterized by a single peak (characteristic of chrysotile) and then a doublet or triplet of dehydration pulses migrating from lower (450–600 °C) to higher (450–700 °C) temperatures as a function of reaction advancement. Specifically, we note a decrease in the weight loss component ranging, from 400 to 540 °C, and an increase in the component between 550 and 700 °C. As mentioned above, the shift in serpentine dehydroxylation range to higher temperatures could be linked to the presence of larger serpentine particles. According to the literature (Cressey and Zussman, 1976; Middleton and Whittaker, 1976; Viti, 2010), indicating that the transition from rolled to flat serpentine will favor dehydroxylation at higher temperatures, the change in TG features from a single peak to a doublet reinforces the supposition of a transition from pure chrysotile to a mix between chrysotile and polygonal serpentine consisting of flat layers of lizardite arranged as an outer shell around the chrysotile core. Phase quantification by TGA, reported in Table 1, is consistent with the spectroscopic and textural identifications described by Lafay et al. (2012).

Based on modal proportion measurements for the serpentine and brucite, serpentinization reaction kinetics were modeled by iterative regression using a pseudo-second order kinetic model (200 fits and 200 iterations) following the equation $\xi_t = \frac{\xi_{max} t}{t_{1/2}+t}$. Here, ξ_t is the reaction extent for a given reaction time t, ξ_{max} is the maximum serpentinization extent (constraint to 100% for the different calculations) and $t_{1/2}$ is the half serpentinization time. We estimated reaction advancement either considering only serpentine modal proportion (as it was done in Lafay et al., 2012) or considering both serpentine and brucite mineral content (Fig. 7 and Table 4). Serpentinization reaction kinetics depends on initial grain size of the olivine, but no significant changes were observed between the 3 systems tested for a similar grain size (30–56 µm).

Under the specific experimental conditions we estimate that As, Sb and Cs have no quantifiable effect on the serpentinization reaction kinetics with respect to FME-free system Our estimations are consistent with results obtained in alkaline FME-free systems where only serpentine mineral abundance was considered (Lafay et al., 2012). Considering both brucite and serpentine mineral abundance and a similar kinetic regime for olivine mineral alteration in As-, Sb- and Cs-rich systems, the average initial rate $v_0 = \xi_{max}/t_{1/2}$ and the $t_{1/2}$ estimated from the calculations are: 3.9 E−06 s^{-1} and about 3 days, 6.65 E−07 s^{-1} and 17.4 days, 1.6 E−07 s^{-1} and 73 days for <30 µm, 30–56 and 56–150 µm initial grain size, respectively. Obviously, the calculations result in a slightly faster reaction kinetic than considering serpentine only. As ξ_{max} asymptote is constraint to 100%, the modeling of mineral abundance

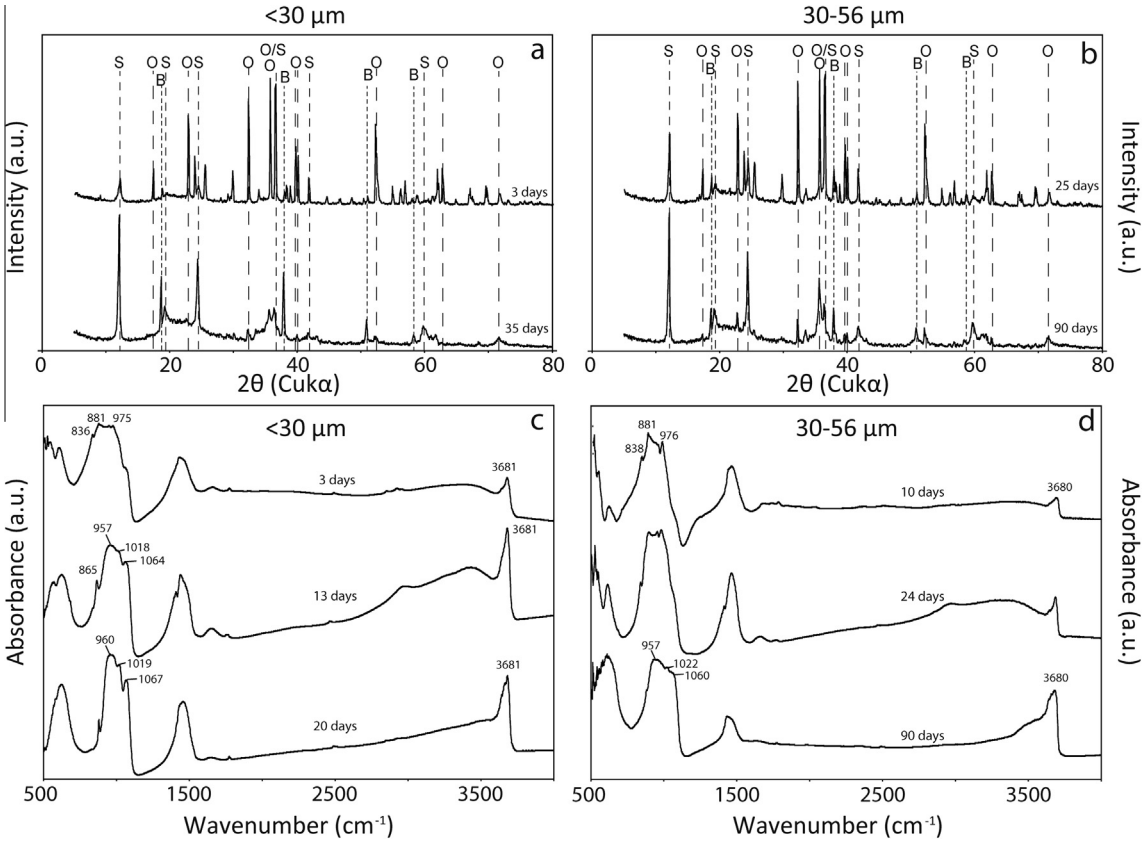

Fig. 3. XRPD diffractograms (a) for As-rich experiments (<30 µm initial grains) and (b) Sb-rich experiments (30–56 µm initial grains) for different reaction times, and FTIR spectra (c) for As-rich experiments (<30 µm initial grains) and (d) Cs-rich experiments (30–56 µm initial grains). Peak position, O: olivine (Forsterite ICDD card #7-74), S: serpentine (chrysotile ICDD card #27-1275) and B: brucite ICDD card #74-2220.

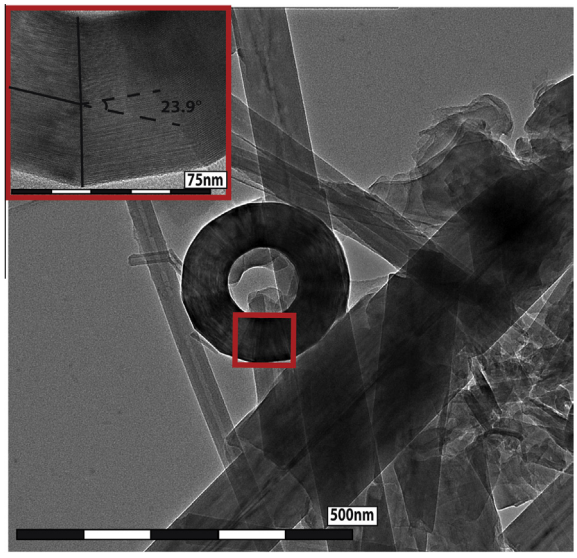

Fig. 4. Transmission electron microscope imaging of chrysotile and polygonal serpentine assemblage precipitated after 90 days of reaction for 30–56 µm initial grain size in As-rich solution (run As-11), inset shows 15-sectored polygonal serpentine with 100 nm wide chrysotile core having disappeared.

remains difficult for longer reaction advancement (and secondary products may be slightly overestimated from TGA measurements).

3.1.3. Iron oxidation state

The Mössbauer spectrum of San Carlos olivine (30–56 µm) is characterized by a single doublet with an Fe centre shift δ of 1.15 mm s^{-1} and a quadrupole splitting Δ of 3 mm s^{-1} (Fig. 8) typical for Fe(II) (De Coster et al., 1963; Delmelle and Gerard, 1964). Fig. 8 displays the Mössbauer spectrum of alteration product after complete serpentinization of San Carlos olivine with no trace elements in the starting experimental fluid. The spectrum is characterized by four doublets typical of two ferrous components ($\delta = 1.15$, $\Delta = 2.93$ and $\delta = 1.04$, $\Delta = 2.98$) and two ferric components ($\delta = 0.26$, $\Delta = 0.52$ and $\delta = 0.35$, $\Delta = 0.82$). The first ferrous component (~30% of total Fe) is related to brucite and the second (~20% of total iron) corresponds to octahedral Fe(II) in serpentine (Blaauw et al., 1979; MacKenzie and McGavin, 1994). Mössbauer spectrum modeling for serpentinized product indicates that under our specific high alkaline conditions, almost half of bulk Fe is Fe(III). Considering both isomeric shift and quadrupole splitting, and regarding the results of the study by Klein et al. (2009) investigating the iron oxidation state

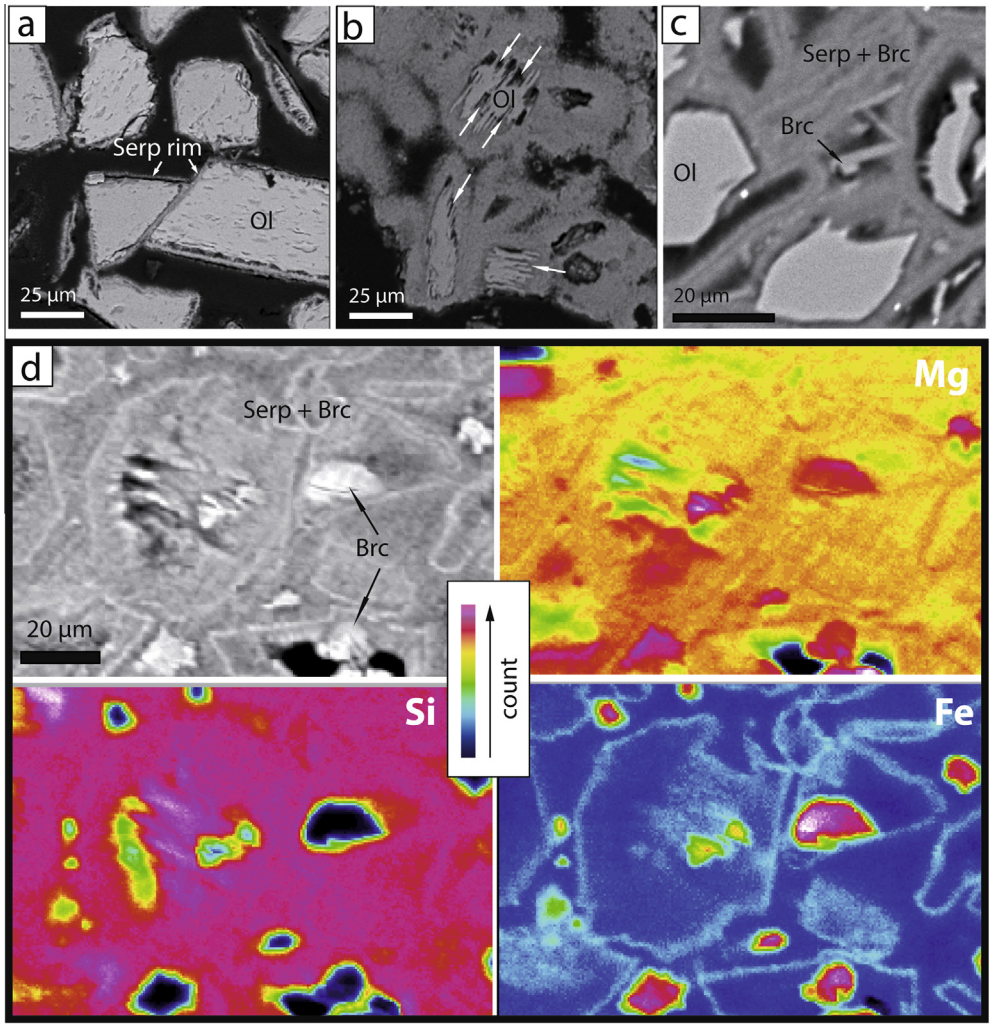

Fig. 5. Scanning electron microscope imaging of the reaction product from olivine alteration, (a) thin serpentine border around olivine grains after 3 days in Sb-rich solution (30–56 µm, run Sb-1), (b and c) notches developed in olivine grains and porous serpentine/brucite assemblages after 41 days in presence of As-rich solution (run As-8), (d) SEM imaging and corresponding EMP mapping for Mg, Si and Fe for experiments after 50 days of reaction in presence of Cs-rich solution (run Cs-4).

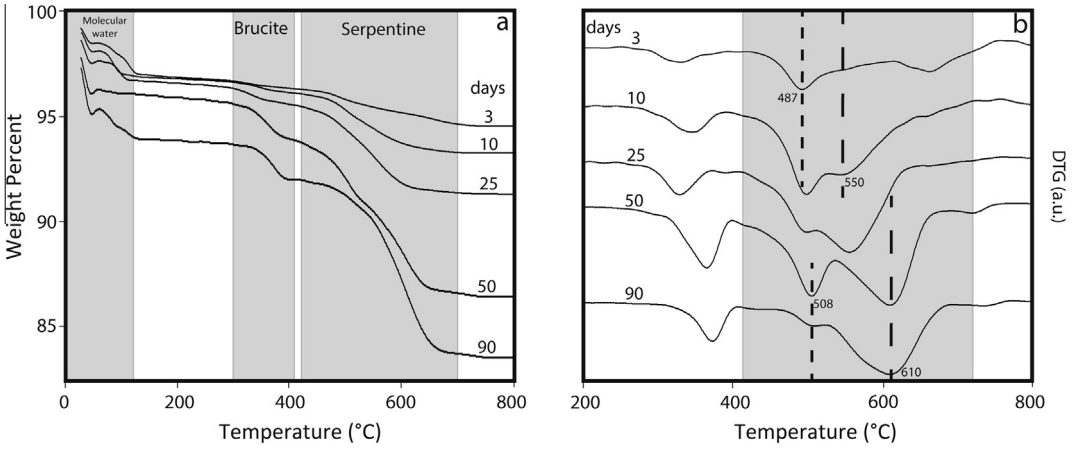

Fig. 6. (a) Typical thermal analyses, example for Sb-rich series samples (30–56 µm initial grains) for different reaction times (air atmosphere, heating rate 10 °C min^{-1} and temperature range 0–800 °C) and (b) corresponding DTG revealing the change in serpentine component properties.

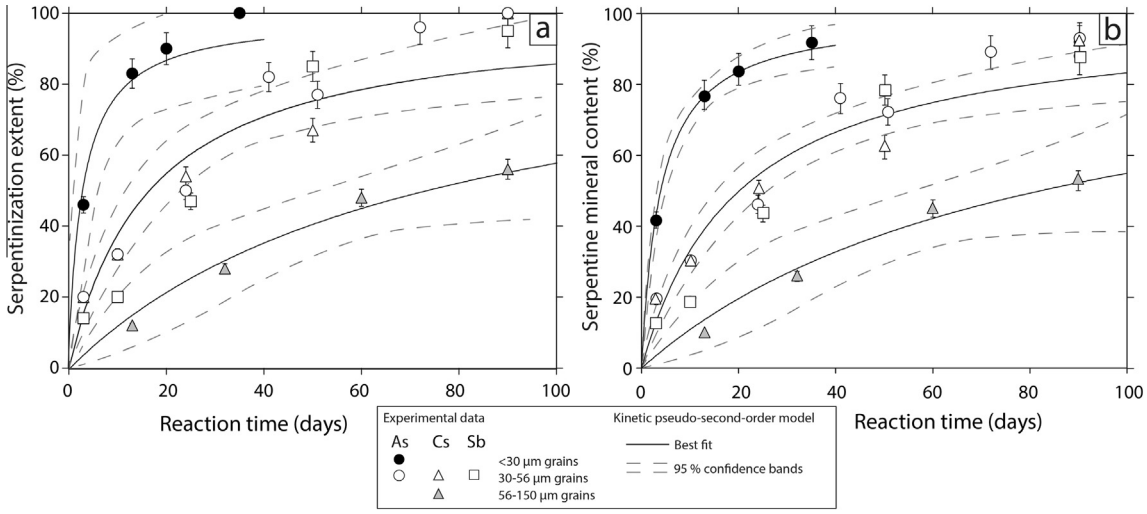

Fig. 7. Mineral abundance (deduced from TGA/DTG measurements) versus time for different olivine grain sizes reacting with As-rich (circle), Sb-rich (square), or Cs-rich (triangle) solution, (a) including serpentine + brucite content and (b) using serpentine abundance only. Best fit for pseudo-second order kinetic models using parameters reported in Table 4 are also represented (solid lines) as well as the 95% prediction bands (dotted lines) which accounts for uncertainty and scattering of data during the fitting.

Table 4
Summary of kinetic parameters calculated from thermogravimetric analyses.

Initial olivine size (µm)	ξ_{max} (%)*	$t_{1/2}$ (days)	v_0 (1/s)	Fitting r^2
Using chrysotile + brucite mineral content contenabundance				
<30	100 ± 5	2.95 ± 0.7	$3.9 \times 10^{-6} \pm 0.7 \times 10^{-6}$	0.97
30–56	100 ± 9	17.4 ± 5	$6.8 \times 10^{-7} \pm 1.5 \times 10^{-6}$	0.94
56–150	100 ± 22	73 ± 30	$1.6 \times 10^{-7} \pm 0.5 \times 10^{-7}$	0.99
Using chrysotile mineral content				
<30	100 ± 2	3.9 ± 0.4	$3 \times 10^{-6} \pm 0.4 \times 10^{-6}$	0.99
30–56	100 ± 8	20 ± 5	$5.8 \times 10^{-7} \pm 2.5 \times 10^{-7}$	0.96
56–150	100 ± 27	82 ± 39	$1.4 \times 10^{-7} \pm 3.4 \times 10^{-7}$	0.98

* Kinetic parameters are calculated using experimental data from Table 1 and following the nonlinear equation: $\xi_t = \frac{\xi_{max} t}{t_{1/2}+t}$ with ξ_t, the reaction advancement (%), for a given reaction time t, ξ_{max} the maximum alteration extent constraint to 100% and $t_{1/2}$ the half reaction progress time and $v_0 = \xi_{max}/(t^{1/2} * 100)$ the initial reaction rates. The values obtained using only the chrysotile mineral content can directly be compared kinetic with values from Lafay et al. (2012).

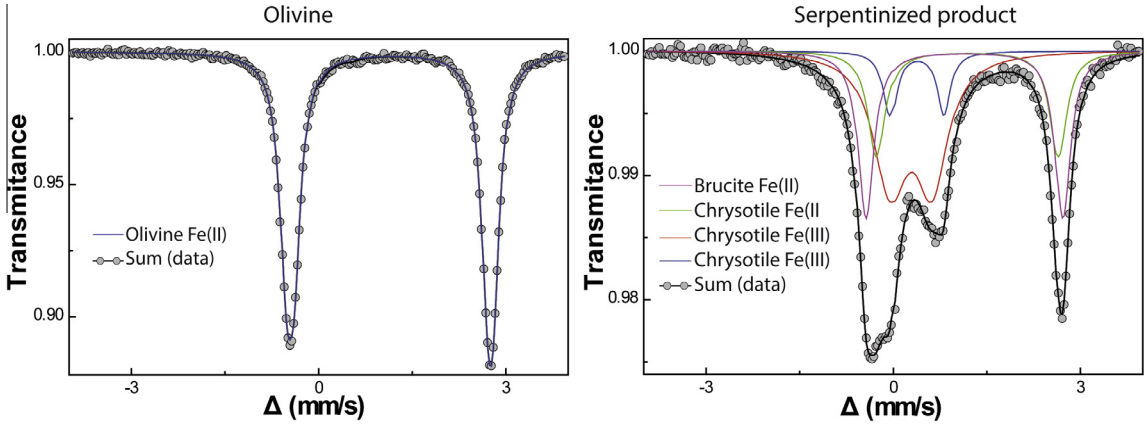

Fig. 8. Mössbauer spectrum obtained at 77°K, on ferrous San Carlos olivine (left) characterized by high quadrupole splitting typical of Fe(II), and on alteration product (right) characterized by two ferrous components (brucite Fe(II) (purple) and serpentine octahedral Fe(II) (green)) and two ferric components (octahedral (red) and tetrahedral (blue) Fe(III) in serpentine). (For interpretation of the references to color in this figure legend, the reader is referred to the web version of this article.)

during serpentinization, the two ferric components were attributed to octahedral Fe (~40% of total Fe) and tetrahedral Fe (~10% of total Fe) in the serpentine. Neither Fe(II) nor Fe(III) component related to magnetite was observed. Thus at 200 °C, despite the absence of magnetite precipitation, the bulk Fe(III)/Fe(II) is approximately 1 after complete experimental olivine serpentinization. Iron is incorporated by Fe-rich brucite containing around 18 wt. % of Fe as Fe(II) and serpentine that contains 6–11% of Fe with a substantial amount a ferric iron ($Fe(III)/Fe_{Total(serp)} \sim 0.7$). The $K_D = (X_{Fe}/X_{Mg})Srp \times (X_{Mg}/X_{Fe})_{Brc}$ is about 0.44. It should be borne in mind that this represents the final state for iron, Fe(III)/Fe(II) in the reaction product having evolved throughout the reaction.

3.2. FME behavior during serpentinization

3.2.1. Bulk FME concentration

Table 1 and Fig. 9 report the results of the bulk-rock measurements on the bulk experimental material as well as calculated concentrations for experimental product (serpentine and brucite only). The results indicate that the three elements where efficiently trapped by the experimental product but in a different range of concentrations and following a different pathway. From bulk rock ICP-MS measurements (including serpentine ± brucite ± residual olivine) and the advancement of serpentinization, we estimated the amount of FME in the alteration product (i.e. serpentine + brucite only, Fig. 9b, d and f), and estimated the partitioning coefficient between reaction product and fluid $^{FME}D_{p/fl}$, (Table 1).

Arsenic content in the experimental product increases linearly from 100 ppm (degree of serpentinization ≈ 30%) to 610 ppm for total replacement whereas the As concentration rises from 500 ppm (≈50% replacement) to 1090 ppm (total replacement) for the smallest initial grain size experiments (Fig. 9a). When these data are converted to As concentrations in the alteration products, it appears that As slightly decrease from ~880 μg g^{-1} after 3 days of reaction to ~600 μg g^{-1} after 40 days of reaction using an intermediate initial grain size (30–56 μm) and remains almost the same in the last stage of the reaction (Fig. 9b). This results in a distribution coefficient $^{As}D_{p/fl}$ that remains nearly unchanged and comprise between 3.5 and 4.5. Despite the lack of data before 50% of reaction for the <30 μm grain size, the As concentration value in alteration products appears to remain close to 1200 μg g^{-1}, which corresponds to an $^{As}D_{p/fl}$ of 8.6 after complete reaction.

Cesium concentrations in the bulk experimental products are comprised between 108 and 181 μg g^{-1} (11–55% replacement) for 56–150 μm and from 192 to 269 μg g^{-1} (19–100% replacement) for 30–56 μm initial grain sizes (Fig. 9c). These results correspond to a nonlinear decrease in the concentration of Cs sequestered by serpentine and brucite as a function of the progress of serpentinization (Fig. 9d). The average Cs concentration in the alteration product highly decreases during the first step of the reaction, from 1050 (20% replacement) to ~500 μg g^{-1} (50% replacement) starting with 30–56 μm olivine grains and from 1000 (15% replacement) to 330 μg g^{-1} (50% replacement) starting with 56–150 μm grains. In the latter case, assuming the trend is correct, the value should be lower than 300 μg g^{-1} after the reaction is complete. These results outline a decrease in $^{Cs}D_{p/fl}$ from 5 to 1.5 with progressive advancement of the serpentinization reaction (from 15% to 50% replacement), with minor difference between the two experimented grain fractions after 50–60% of replacement (Fig. 7).

Antimony concentrations in the experimental products (30–56 μm olivine grains) greatly increase during the first stage of the reaction from ~500 μg g^{-1} after 3 days to 2000 μg g^{-1} (Fig. 9e) after 25 days (~47% replacement). The Sb bulk concentration then remains nearly the same (~2000 μg g^{-1}), forming a concentration plateau. These observations correspond to a two-stage behavior for Sb partitioning with first, an increase in average Sb concentration in the alteration product from 3900 to 4500 μg g^{-1} (up to 50% replacement) and then a substantial decrease from 4500 to 1900 μg g^{-1}. Corresponding estimated $^{Sb}D_{p/fl}$ increases from ~20 to ~65 from 3 to 25 days of reaction. This corresponds to the trapping of the majority of the Sb by reaction product prior to a decrease in $^{Sb}D_{p/fl}$ from ~65 to ~28, suggesting that bulk Sb sequestration decreases or stops after 25 days of reaction, this probably linked to a change of sequestration processes.

3.2.2. Spatial distribution of FME

In X-ray maps, Fe appears heterogeneously distributed in serpentine mineral with the highest apparent Fe content found in serpentine that formed at the pristine grain boundaries of olivine (Fig. 10) and the lowest content in the serpentinized core. Keeping in mind that the bulk Fe spatial distribution is also probably linked with heterogeneous distribution of Fe(II)/Fe(III). Single brucite grains and/or brucite aggregates are readily recognizable on X-ray mapping by their high Mg and Fe content with no Si (Figs. 4, 10 and 11). The presence of aggregate of brucite minerals in the most advanced experiments suggests for possible chemical segregation and mineral coarsening by dissolution/precipitation throughout the serpentinization reaction (Oswald ripening). Quantitative measurements (EPMA) reveal that brucite grains are characterized by a high Fe content with respect to serpentine (Figs. 5d, 10 and 11). Assuming all Fe to be divalent, EPMA give 6–11 and 14–25 wt.% for FeO in serpentine and brucite respectively (Table 2 and 3).

Arsenic X-ray maps for an advanced reaction (e.g. 90 days starting from 30–56 μm grain size) display a higher As content in brucite (Fig. 10a) than in serpentine and olivine residual. Indeed As quantities in residual olivine are below the detection limit (Tables 2 and 3) but are between 300 and 1000 μg g^{-1} in serpentine and between 1400 and 3000 μg g^{-1} in brucite. Yet, brucite is not enriched with other minor elements (Ni, Cu, Cr, etc.). Based on the serpentine and brucite amounts in the serpentine product, the in-situ quantitative concentrations are consistent with those measured by ICP-MS on the bulk serpentine products (600 μg g^{-1} for As starting with 30–56 μm grain size). We report the presence of sparse sub-micrometric As-rich phases (Fig. 10a) containing large amounts of Ni

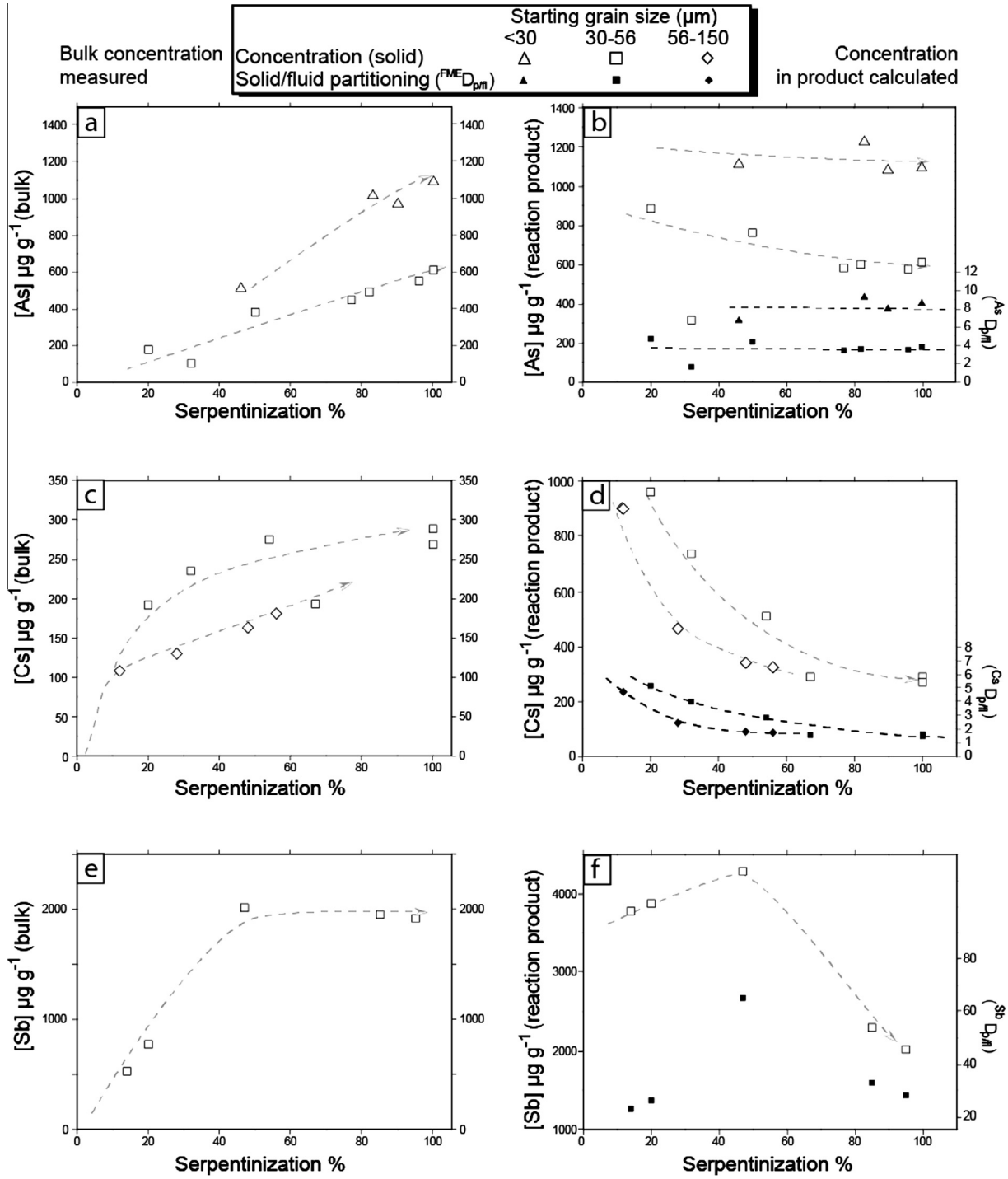

Fig. 9. Concentration of FME in bulk solid product (left) and corresponding average concentration in experimental product (right: serpentine + brucite) as a function of reaction advancement (open symbols) and for the different experimental grain sizes. Concentrations calculated for FME in residual fluid are also reported (filled symbols): (a and b) results for As, (c and d) for Cs and (e and f) for Sb, partitioning trends are represented with dotted arrows.

(0.6–11 wt.% Table 3) but displaying no specific correlation between Fe and As. They may represent hydrated arsenates such as annabergite [$Ni_3(AsO_4)2{\cdot}8H_2O$] but also little As-clusters adsorbed at the serpentine surface (Table 3).

Quantitative measurements for Cs are below detection limit, nevertheless, Cs mapping suggests lower content at serpentinized grains core with respect to borders (Fig. 10b) and no correlation with Fe and Ni. No Cs-bearing phases were observed whatever the initial grain size used in the experiment and the advancement of the serpentinization process.

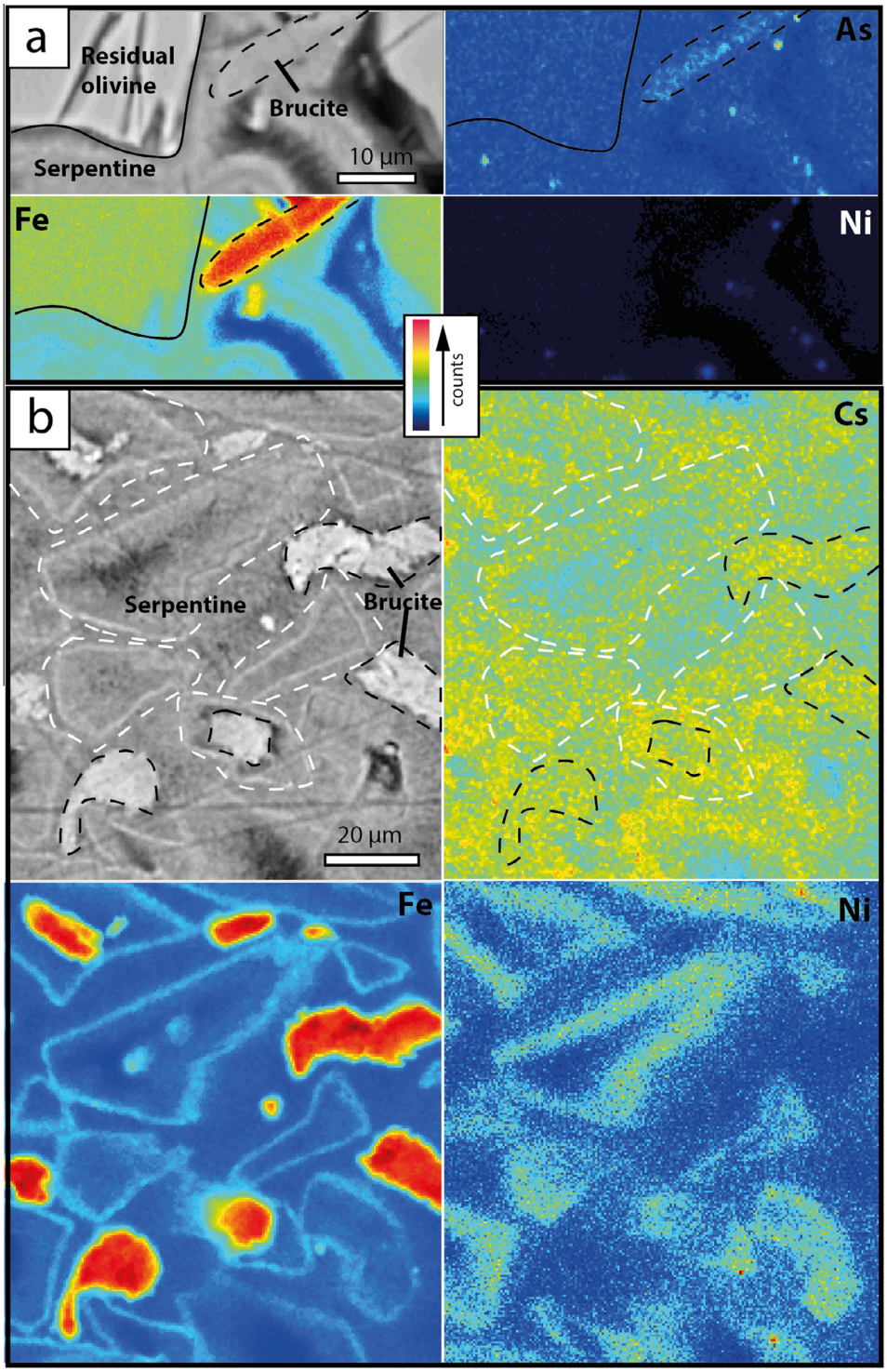

Fig. 10. (a) SEM imaging of As-rich altered product, and corresponding EMP mapping for Fe As and Ni after 72 days of reaction starting with 30–56 µm grain size (run As-10). (b) SEM imaging of Cs-rich altered product, and corresponding EMP mapping for Fe, Cs and Ni after 90 days of reaction starting with 30–56 µm grain size (run Cs-5).

The distribution of Sb correlates very well with the distribution of Ni in the serpentinization product (Fig. 11). This is particularly remarkable after long reaction times, where a collar of Ni- and Sb-rich serpentine minerals is found as relic of the pristine grain borders. As for As, we report no spatial correlation between Sb and Fe. Abundant amounts of Sb-rich phases are observed in serpentinized products in the case of advanced reactions (>50%

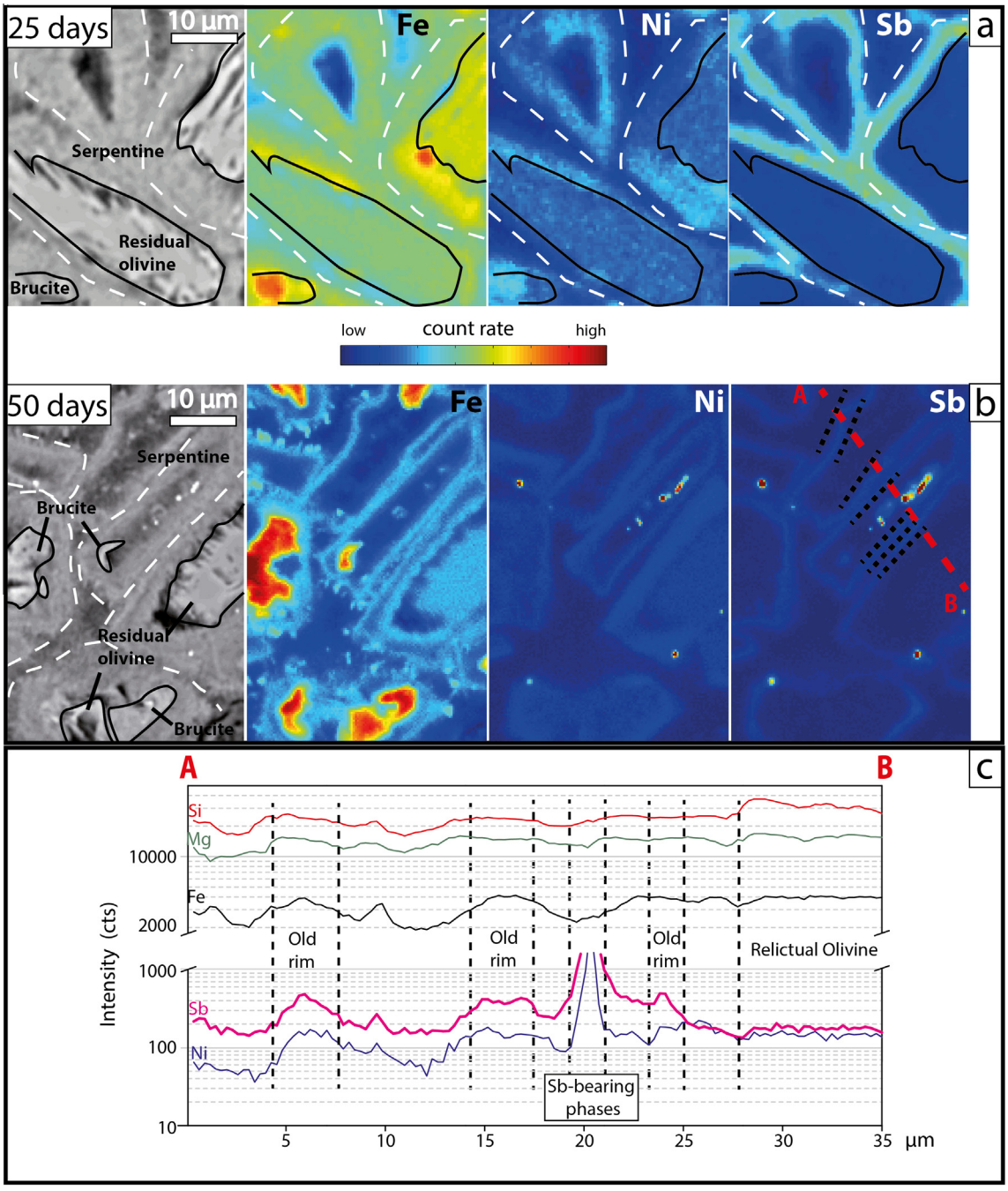

Fig. 11. (a and b) SEM imaging and corresponding EMP mapping for Fe, Sb and Ni from 30–56 µm initial grain size experiments in presence of Sb after 25 days of reaction (run Sb-3) and 50 days of reaction (run Sb-4). The presumed former grain boundaries are reported with dotted white lines, the color scale for count rate is not the same for each map, (b) example of Sb-count (cts) intensity section measured by EMP cross-cutting serpentinized grains (A-B profile in (b)). Note the presence of Sb-enriched serpentinized grain borders and Sb- Ni-rich microphases after 50 days of reaction. (For interpretation of the references to color in this figure legend, the reader is referred to the web version of this article.)

replacement, Fig. 11b). The Sb content of these phases is difficult to estimate due to their sub-micrometric size. Indeed, microprobe measurements overlap with those of serpentine, but show that Sb-bearing phases contain more than 40 wt.% of Sb_2O_3 (Table 2) and about 6 wt.% of NiO but are not characterized by abnormal amounts of Fe (8–10 wt.% oxides) with respect to serpentine. Else, data treatment using oxides exceeds 100% for microprobe analyses suggesting that Sb and Ni are at least partly in their metallic form in these Sb-rich phases. Since Ni/Sb-rich phases were not observed in less advanced experiments, we can be sure that these microphases are not related to a

bias in quenching and/or incomplete washing. The Sb semi-quantitative measurements for Sb in serpentine are mainly comprise between 1600 and 8400 μg g^{-1}, with the highest concentrations at the periphery of the sub-grain domains. This is confirmed independently from mapping (Fig. 11a and b) and by elementary profiles through the serpentinized product (Fig. 11c) and isolated measurement. Indeed, the value of 67 ppm corresponds to measurements taken in the centre of serpentinized grains. Pure brucite contains no Sb (<330 μg g^{-1} when mixed with serpentine, Table 2). These results indicate a completely different process for the sequestration of Sb with respect to As and Cs.

3.2.3. Speciation of As and Sb

The normalized XANES spectra collected at the As K-edge and Sb K-edge for the different degrees of advancement of olivine alteration in the presence of 200 ppm of dissolved As or Sb are reported in Fig. 12a and b respectively. Normalized XANES spectra for the three references used in this study are also reported for the sake of comparison.

XANES measurements display no change in the As K-edge region (Fig. 12a) with the degree of serpentinization. E_0 for all the samples remains at the same energy (~11,873.4 eV) and, with respect to the standards, is typical of As(V). This suggests that the As valence state remains unchanged. Moreover, no change in As coordination number and intensity are observed from EXAFS region analysis (Fig. 13). The lack of second and third neighbors in the FT indicates that As(V) is apparently adsorbed by an inner-sphere adsorption mechanism in the experimental products. Hence, the structural incorporation of As in serpentine products including brucite or secondary As-bearing phases (possibly represented by annabergite) seems negligible with respect to the overall As adsorption at the surface of the serpentinization products (serpentine and brucite).

XANES spectra for the two Sb(III) standards display an absorption edge E_0 at 30,494.2 and 30,494.5 eV for $SbCl_3$, Sb_2O_3 respectively, whereas the absorption edge is located at 30,492.7 eV for Sb^0 (Fig. 12b). Absorption edges for Sb-doped samples are systematically located at higher energy levels than the investigated standards. The peak is typically at 30,498.2 eV in the case of small degree of serpentinization (OlSb0a) and at 30,496.2 eV after the reaction is complete. These results provide two sorts of information. First the higher absorption energy is attributed to the presence of pentavalent Sb in the experimental product. Second, the non-negligible continuous shift of E_0 to a lower energy level after 25 days of reaction (reaction progress ~47%) up to complete reaction, underlines a change in Sb valence throughout the experiment. Depending on the EXAFS region, we note no change in Sb coordination number and first neighbor positions during the first 10 days of the reaction (Fig. 14b). The lack of secondary neighbors suggests that Sb(V) trapping is controlled by an inner-sphere

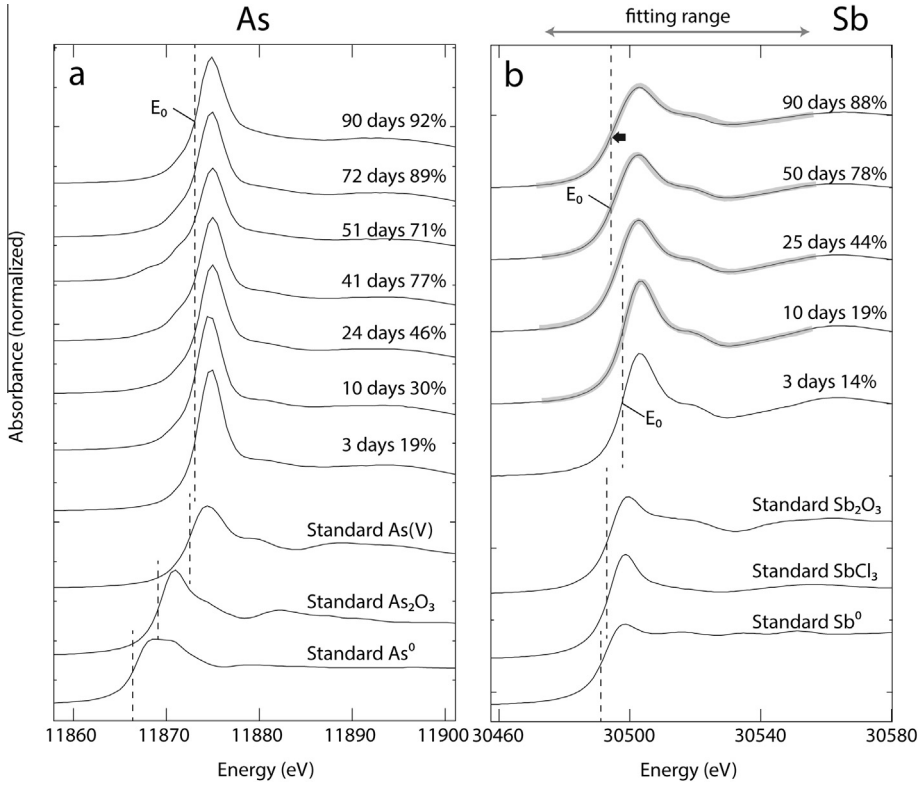

Fig. 12. Normalized As-K pre-edge (a) and Sb-K pre-edge, (b) XANES spectra as a function of energy for the different experimental products and corresponding standards for As-rich series (a) and Sb-rich series (b) respectively. Solid lines represent the experimental data and reaction times with corresponding reaction advancement are also reported. Dotted lines represent E_0 positions and gray lines (b) represent fits using linear combination over the specified fitting range using three Sb standards ($^{\alpha}$ values from Table 5). For more details refer to the text.

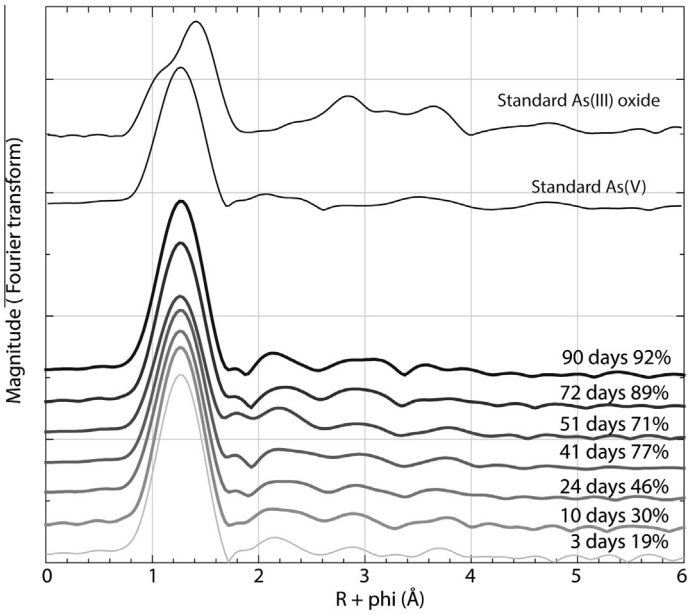

Fig. 13. Normalized k^2-weighted transmission As K-edge EXAFS spectra for As-rich series and As(III) and As(V) standards.

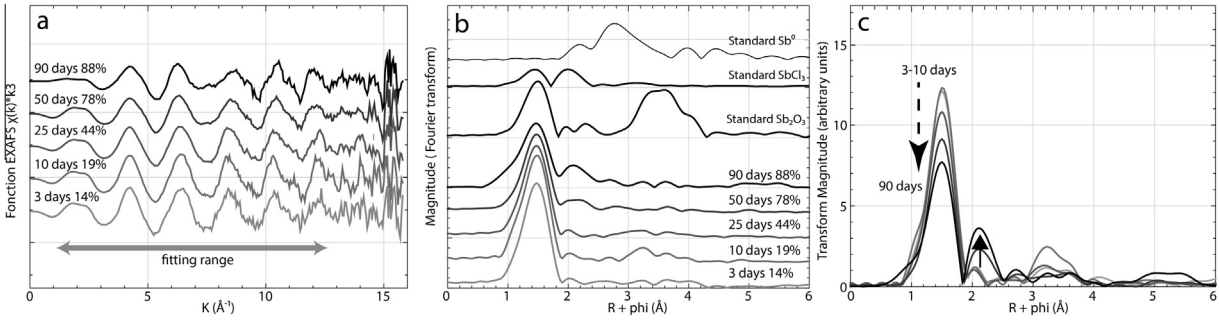

Fig. 14. (a) Normalized k^2-weighted transmission Sb K-edge EXAFS spectra for Sb-rich series and (b and c) their corresponding Fourier transform (FT) magnitudes (χ(R + phi)) corresponding to the radial distribution function as a function of distance from the central antimony atom not corrected for phase shift, respectively, (b) shifted along the vertical axis (compared with acquisitions on Sb(III) and Sb^0 standards) and (c) superposed for better observation of the trend (vertical arrows indicate the decrease (dotted) of first O component and increase (solid) of second component).

adsorption mechanism as in the case of As. After 10 days of reaction (OlSb1a) we observed the first appearance of a second component at (R + phi = 3.25 Å) that matches with oxide standards (Fig. 14b), but as no shift in E_0 was observed between 3 and 10 days, we infer that it may correspond to the presence of small amounts of transient Sb(V) oxides. After 24 days of reaction, the Sb first neighbor component decreases significantly, indicating a change in Sb coordination (Fig. 14c). This is related to the emergence of a secondary component that matches with the $SbCl_3$ standard at 2.11 Å (uncorrected for phase shifts) and grows progressively with the degree of serpentinization. We cannot exclude that minute of transient oxide phase precipitates after 10 days of reaction regarding the second coordination component that emerge at 3.2 Å (uncorrected for phase shifts).

The Sb bulk oxidation state was estimated by linear combination modeling of the XANES (30,460–30,560 eV range, Fig. 12b) and EXAFS (1–13 $Å^{-1}$ region). Four Sb-"end-members" were used Sb(III)-oxide and Sb(III)-chloride, Sb(0) standard, as well as the first sample of the (OlSb0a) series, which was assumed to be a Sb(V) component. Different fits were performed using Sb(V) and Sb(III) only and using Sb(V), Sb(III) and Sb(0). Examples of proportions calculated are displayed in Table 5. Both models match and are comparable whatever the Sb(III) standard. Our results indicate that about 30% of Sb(V) is reduced to Sb(III) after 25 days of reaction. After complete reaction, only 50% of initial Sb(V) remains present in solution. Therefore the bulk solid system is characterized by the presence of Sb(V), Sb(III) and possibly metallic Sb(0). After 25 days and until the end of the reaction, Sb is significantly trapped in Ni- and Sb-rich phases, which might correspond to pure end-member or mixture of chloride ($(Ni,Sb)Cl_3$), valentinite (Sb_2O_3), breithauptite (NiSb) or nisbite ($NiSb_2$). EMPA show no evidence for linkage between Cl and Sb, indicating rather for Sb precipitation as oxides or alloys.

Table 5
Results of linear combination of XANES and EXAFS regions at the Sb K-edge for Sb-doped samples.

	Component (%)				Reaction time
	XANES region	EXAFS region	XANES region	EXAFS region	(days)
	Sb-1		$SbCl_3$		
Sb-1	100	100	0	0	3
Sb-2	100	100	0	0	10
Sb-3	72.4	67.5	27.6	32.5	25
Sb-4	59.5	40.5	49	35.9	50
Sb-5	54.1	52	45.9	48	90
$SbCl_3$ [β]	0	0	100	100	–

	Component (%)			Reaction time
	XANES region			(days)
	Sb-1	Sb_2O_3	Sb0	
Sb-1	100	0	0	3
Sb-2	100	0	0	10
Sb-3	67	34	0	25
Sb-4	54	34	12	50
Sb-5	49	13	37	90
Sb0	0	0	100	–

[β]Considering run Sb-1 and $SbCl_3$ as standards.
[α]Considering run Sb-1, Sb_2O_3 and Sb0 as standards.

4. DISCUSSION

4.1. Reaction mechanism and evolution of serpentinization reaction

In natural serpentinites, the typical olivine alteration reaction involves mass transfer of Si, Fe and Mg, and leads to the formation of characteristic serpentine mesh textures (olivine pseudomorphosis) surrounded by magnetite that highlight former (sub)grain boundaries (Wicks and Whittaker, 1977). The presence of magnetite is due to the removal in solution and oxidation of the Fe(II) originally contained in olivine (Allen and Seyfried, 2003; Bach et al., 2006; Seyfried et al., 2007). This reaction leads inherently to reducing conditions during the serpentinization reaction (Frost, 1985), which in turn can affect the behavior of the redox-sensitive minor and trace elements (Ballhaus, 1993; Andreani et al., 2013), and cause the precipitation of metallic mineral and/or sulfide deposits (Rona, 1984; Frost, 1985; Alt et al., 2013). At low alteration temperatures (<200 °C), magnetite is generally lacking (Klein et al., 2009, 2014; Lafay et al., 2012; Andreani et al., 2013; Evans et al., 2013) but brucite is found commonly (Allen and Seyfried, 2004; Lafay et al., 2012). The absence of magnetite does not necessarily reflect the absence of Fe (III), but only that it is redistributed in serpentine minerals and brucite (Klein et al., 2009, 2014). The presence of coarse brucite and brucite-rich rims reflects the discrepancy between brucite and serpentine supersaturation related to olivine alteration (Klein et al., 2009).

In our experimental system, we used a powder consisting of individual olivine grains but alteration textural features similar to those reported in natural systems were reproduced. The typical olivine replacement textures include a clear serpentinization front, the presence of notches at the reaction interface, and the development of sub-grains by a fracturing process (Fig. 5; Iyer et al., 2008). Under this high alkaline environment at 200 °C, no iron oxide is formed during alteration and olivine is replaced by the typical low-temperature assemblage composed of serpentine and brucite (Allen and Seyfried, 2004; Lafay et al., 2012; Klein et al., 2014). Here, Mössbauer's results confirm that about half the Fe(II) originally contained in the olivine is oxidized and preferentially incorporated into the serpentine minerals. The remaining Fe(II) is trapped mainly by brucite (~30% of total iron) and serpentine (~20% of total iron). Thus, our static system is a characteristic example where redox development appears to be controlled by a (Fe(II)/Fe(III)-serpentine)/(Fe(II)-brucite) buffer and the presence of H_2-bearing fluids despite the lack of magnetite. Our results are in agreement with the mean values for $K_D = (X_{Fe}/X_{Mg})_{Srp} \times (X_{Mg}/X_{Fe})_{Brc}$ reported in the literature (0.5) for brucite–serpentine assemblages (Evans and Trommsdorff, 1972; Klein et al., 2009).

In the experimental conditions, the reaction kinetics is faster than in the case of serpentinization in neutral conditions (at least 10 time faster referring to Malvoisin et al., 2012), and is dependent of the initial olivine grain size (Lafay et al., 2012). Here, the textural properties (dimensions, morphology) of the serpentinization product appear to be vicariously related to the grain size of the initial olivine and the progress of the reaction. Indeed, experiments using the smallest starting grain size with the fastest replacement kinetics lead to the formation of the smallest chrysotile–brucite particles. Furthermore, a longer reaction time favors the growth of larger serpentine fibers (including polygonal serpentine). The starting grain size also affects the thickness of the serpentinization product and thus the ease with which fluids percolate up to and are disposed of on the surface of the olivine. The textural development of

the experimental products may account for the bending in the pseudo-second order kinetic curves (Fig. 7).

4.2. Solid/fluid distribution and sequestration mechanism of As, Cs and Sb during olivine serpentinization

Under the experimental conditions investigated here, the solid/fluid partition coefficients (FMEDp/fl) estimated from the FME concentrations in the experimental products (ICP-MS) are systematically higher than 1. The typical sequence determined for an initial olivine grain size of 30–56 μm is: $^{Cs}D_{p/fl} < {}^{As}D_{p/fl} < {}^{Sb}D_{p/fl}$ after the reaction is completed (Table 1 and Fig. 9). Although it was observed that serpentinization products effectively trap As, Cs or Sb, the combination of geochemical measurements (FME concentrations in serpentine products) and accurate analytical techniques (including high-resolution in-situ techniques) reveals not only the different affinities of FME for serpentine and brucite but also three distinct behaviors.

4.2.1. Arsenic

Arsenic trapping by alteration products remains almost the same throughout the olivine serpentinization process, suggesting that the partitioning mechanism remains unchanged as the reaction progresses (Fig. 9b). Arsenic seems to be homogeneously distributed in the serpentine minerals (300–1000 μg g^{-1} from semi-quantitative EPMA), and brucite typically retains 3–5 times more As compared with serpentine (1400–3000 μg g^{-1} from semi-quantitative EPMA). The preferential As sequestration at the brucite surface is compatible with results found in the literature (Yang et al., 2005; Bochkarev et al., 2010; Opiso et al., 2010), showing that Layered Double Hydroxides (LDH) with brucite-like octahedral layers constitute good adsorbents for As (Yang et al., 2005). The preferential As sequestration from brucite with respect to serpentine may account for the larger $^{As}D_{p/fl}$ (4–9) compared with the chrysotile/fluid partition coefficient of 2.6 determined on pure Mg-chrysotile synthesized from a fluid solution at 300 °C under alkaline conditions (Lafay et al., 2014).

In light of the XANES measurements, we propose that the state of oxidation of As(V) remains unchanged throughout the reaction and, thus, the conditions for As(V) reduction into As(III) were not achieved in the course of the serpentinization reaction. Furthermore, EXAFS results indicate that As bonding remains characterized by strong first-oxygen coordination. The absence of a secondary neighbor for As(V) suggests that adsorption mechanisms control As trapping by serpentine products (serpentine and brucite). An adsorption mechanism may also account for the variation in the amount of As trapped in serpentine depending on the initial grain size. Indeed, a change in the variety and textural properties of the serpentine minerals affects As trapping ability: chrysotile (small olivine grain size and fast kinetics) seems much more able to trap As ($^{As}D_{p/fl} \sim 8$) than mixed chrysotile/polygonal serpentine (larger grain size and slower kinetics and $^{As}D_{p/fl} \sim 4$).

Although precipitation of minute As-rich microphases was observed by 2D chemical analysis, we propose that the As-rich phases probably play a minor role on the As budget as spectroscopic EXAFS measurements reveal a single adsorption mechanism with no contribution related to structural As. This appears to be confirmed independently by mass balance calculations based on As concentrations measured in serpentine and brucite mineral that account well for the bulk As concentrations measured in the reaction product (using modal abundance determined by thermogravimetry).

4.2.2. Cesium

Cesium is the FME with the lowest uptake by serpentinization products. Cesium concentrations in serpentine products are too low to distinguish the respective distribution between serpentine and brucite by EMPA. In contrast to As, no secondary phase was observed.

The slight decrease in sequestration with increasing grain size (Fig. 9c and d) suggests here again that there is a single adsorption mechanism for Cs trapping in serpentine products. Remarkably, the solid/fluid partition coefficient clearly decreases throughout the reaction (from ~5 to ~1.5) with both initial grain sizes investigated. Since Cs is the investigated FME with the lowest $^{Cs}D_{p/fl}$, the progressive decrease in Cs trapped in serpentine products during the experiment cannot be explained by a modification in the FME concentration in the experimental fluid. Therefore, it is proposed that Cs is preferentially trapped in the incipient stages of alteration, probably at the interface between the solution and the border of the replaced grains. Coarsening of the serpentine minerals and/or an Ostwald ripening mechanism might cause a change in partitioning. Moreover, the fluid percolating from the free medium to the surface of the olivine through the serpentinized front may undergo progressive Cs depletion, and the amount of Cs trapped by serpentine will decrease as the reaction progresses. This might lead to the formation of a concentration gradient from the mesh border to the core. Preferential enrichment at the mesh border is observed in the case of Li (an element with a similar electronic charge to Cs) during natural olivine replacement (Benton et al., 2004; Pabst et al., 2011). The large difference in terms of charge, preferential coordination (octahedral for Cs(I) and both octahedral and tetrahedral for As(V)) and ionic radius size (1.67 and 0.35 Å for Cs and As respectively, Shannon, 1976) could explain the differences between As and Cs migration and sorption in the serpentinized product. As serpentinization is linked to expansion and diffusion of major elements (Kelemen and Hirth, 2012), diffusion processes can also appear to redistribute As during grain coarsening.

4.2.3. Antimony

Antimony distribution changes considerably as hydrothermal alteration progresses. The incipient reaction favors a high $^{Sb}D_{p/fl}$, which rapidly increases (from 22 to 65, Table 1 and Fig. 9e, f), indicating that a significant amount of Sb is removed from the fluid (66 mg L^{-1} residual Sb in fluid after 47% of serpentinization) by neo-formed serpentine products. EMPA reveals that serpentine contains at least 5 times more Sb than brucite. XANES results indicate that the first stages of the reaction are marked by prompt oxidation of the $SbCl_3$ introduced into the starting

solution (characterized by inner sphere complexes of Sb(III)) in aqueous Sb(V) (Sherman et al., 2000). Antimony(V) seems to be easily removed from the fluid via adsorption by serpentine as can be seen on the XANES spectra of the serpentine products (until about half of the replacement has taken place). Quantitative measurements in serpentine (1500–8000 $\mu g\ g^{-1}$) are in agreement with ICP-MS values ($\sim$4000 $\mu g\ g^{-1}$ on average in serpentization product). During the second stage of the serpentinization reaction (extent of reaction >47%), the decrease in average Sb concentration in the bulk serpentinization products (Fig. 9f), and related $^{Sb}D_{p/fl}$ by a factor of 2 highlights a change in the Sb sequestration mechanism. This change appears to be linked, remarkably, with the reduction from Sb(V) to Sb(III) and apparently Sb(0), as suggested by XANES combined with EMPA on Sb- and Ni-rich microphases. Indeed, reduced varieties of Sb being less soluble (Vink, 1996; Filella et al., 2002a), Sb reduction favors precipitation of accessory phases and in turn partly prevents Sb sequestration by serpentine minerals. Consequently, the late-formed serpentine contains less Sb (Fig. 10) and the partitioning coefficient decreases remarkably. The final estimated $^{Sb}D_{p/fl}$ of about 28 represents a mixture of Sb(III) incorporated in accessory phases and Sb(V) sorbed in serpentine (possibly in the early stage of reaction).

In the experimental system, the oxidation of half of the total Fe(II) originally contained in the pristine olivine (Fig. 8) drives the system towards reductive conditions. Changes in redox conditions related to Fe oxidation have crucial implications with regard to the Sb partitioning mechanism. Indeed, Fe remains the main supplier for electron exchanges and its oxidation appears to be related to the reduction of water and minor/trace elements such as Sb; Sb(V) reduction following for example the coupled redox reactions: $2Fe(II) \Rightarrow 2Fe(III) + 2e^-$ and $Sb(V) + 2e^- \Rightarrow Sb(III)$. Consequently, whereas Sb(V) is adsorbed by serpentine during the incipient reaction, we propose that reduced Sb (Sb(III) and possibly Sb(0)) is mainly contained by Ni- and Sb-rich accessory phases. While the use of high pH enhances Sb aqueous species solubility (mainly as SbO_3^- and $Sb(OH)_6^-$ for high pH and oxidizing conditions), the reduction of Sb is linked to a decreasing of it solubility in aqueous solution (Vink, 1996; Filella et al., 2002a; Helz et al., 2002). In our experimental system, the precipitation of secondary Ni- and Sb-rich accessory phases is enhanced by the high Sb-concentration of the starting solution.

In natural systems the precipitation of FeNi oxides and metallic phases was recognized for reducing conditions (Eckstrand, 1975; Sleep et al., 2004; Plümper et al., 2014) but the occurrence of trace element is rarely discussed and Sb-rich alloy is only addressed for ore-deposit systems (e.g. Cook, 1996). However it is also recognized that Sb might be adsorbed by metallic oxy-hydroxide (Thanabalasingam and Pickering, 1990; Filella et al., 2002a).

Interestingly we note that the appearance of Ni–Sb accessory phases limit Sb adsorption by serpentine, after reaction is 50% complete. After complete reaction, the total Sb uptake in Sb(V) adsorbed at the surface of serpentine remains higher than total reduced Sb that precipitated as a microphase.

4.3. Implications for FME distribution in natural hydrothermal systems

4.3.1. Concentrations in natural serpentinites

Many abyssal serpentinites are enriched in the trace elements studied here in relation to their mantle precursors (Deschamps et al., 2010; Kodolányi et al., 2012; Lafay et al., 2013). Among the investigated FME, As is the most enriched but As, Sb and Cs concentrations never exceed a dozen $\mu g\ g^{-1}$ and are mostly below 1 $\mu g\ g^{-1}$ on average in serpentinite rocks (from the mid-ocean ridge, passive margin and forearc environments). Arsenic concentrations vary in a range of at least 3 orders of magnitude from tens of $ng\ g^{-1}$ to tens of $\mu g\ g^{-1}$, whereas Cs and Sb concentrations are typically reported at 0.1–1 $\mu g\ g^{-1}$ or even below (Werner and Pilot, 1997; Paulick et al., 2006; Deschamps et al., 2012; Kodolányi et al., 2012; Andreani et al., 2014). It should be noted that Deschamps et al. (2010) report even higher As concentrations in forearc serpentinites, ranging up to 80 $\mu g\ g^{-1}$.

Seawater contains very small and homogeneous quantities of FME: typically around 1.7, and 0.3 $\mu g\ L^{-1}$ for As and Cs respectively (Charlou et al., 2002) and about 0.18 $\mu g\ L^{-1}$ for Sb surface oceanic waters (Filella et al., 2002b). Hydrothermal vents where fluids might be compared with the fluid used in the present experiments are found in the Lost City field (fluid temperature beneath sea floor $\sim 200 \pm 50$ °C and pH 9–11 (Proskurowski et al., 2008 and reference therein) but there are no data concerning the As, Cs or Sb compositions for these fluids. Indeed, data concerning hydrothermal fluids where ultramafic alteration is recognized are scarce and are mainly for high temperature (>300 °C) low-pH (below 4) hydrothermal vents. Concentrations reported for these vents compare well from one site to another and the values are systematically higher than those reported for seawater, especially with regard to Cs ($\sim$40–50 $\mu g\ L^{-1}$) (Rainbow, Flores and Logatchev mid-oceanic hydrothermal fields, (Douville et al., 1999, 2002; Charlou et al., 2002; Schmidt et al., 2007). In the Logatchev hydrothermal field, the values for Sb and As are $\sim$0.3–0.9 and 2.8–4.7 $\mu g\ L^{-1}$, respectively (Douville et al., 2002; Schmidt et al., 2007).

As was observed first in the case of pure chrysotile synthesis at 300 °C (Lafay et al., 2014), we confirm in this study that serpentinization products (serpentine and brucite) can efficiently trap up to thousands of $\mu g\ g^{-1}$ of As, Cs and Sb during olivine alteration. This indicates that the limits (saturation) of FME adsorption by serpentinite rocks are clearly never reached in natural systems.

Serpentinization reactions generally occur in open systems out of equilibrium (Bach et al., 2006; Rouméjon and Cannat, 2014) and it is difficult to know whether the serpentinites were at equilibrium with fluids when they were formed and if trace element concentrations measured in fluids leaving hydrothermal vents are representative of serpentinization fluids at depth. However, assuming that the composition of fluids (hydrothermal vents being evidence

of alteration reactions in the oceanic lithosphere) and abyssal serpentinites found in the literature (Werner and Pilot, 1997; Bach et al., 2006; Deschamps et al., 2010; Kodolányi et al., 2012) represents equilibrium concentrations, we can roughly estimate solid/fluid FME partitioning. It is remarkable that there is relatively good agreement between the Cs distribution coefficient (~2.5) calculated using average Cs ~ 0.1 μg g^{-1} in serpentinite and ~45 μg L^{-1} and the experimental value obtained here. In the case of As and Sb, natural solid/fluid FME partitioning remains 1–2 orders of magnitude higher than our results. This difference between the experimental and natural coefficients may have numerous causes including the alteration reaction conditions (T, redox, fluid composition), the serpentinization reaction product (including Fe-oxide and associated alloys), and certainly the lower FME concentrations of natural fluids that will enhance solid/fluid partitioning (Lafay et al., 2014). However, the solid/fluid partition coefficients for all the investigated FME are high (≫1) and, on the basis of our data, we propose that one efficient sequestration mechanism is adsorption on the serpentine products.

4.3.2. Incidence of a prevalent adsorption mechanism

The mechanism of FME trapping in natural serpentinites remains unclear, as FME could either be adsorbed at the mineral surface, structurally incorporated in serpentine minerals or included in accessory phases such as metals or oxides. Since the sites and state of oxidation of As and Sb in silicate and oxide minerals are poorly known, it has been suggested that As(V) and Sb(V) may reside in tetrahedral sites of silicate minerals by replacing Si(IV) (Essozv, 1965; Shannon, 1976).

Although As, Cs and Sb display substantially different pathways, under the specific experimental conditions investigated in this study, we indicate that Cs, As and Sb are preferentially adsorbed at the surface of the serpentine products. We infer that the anti-correlation between the initial grain size and the bulk $^{FME}D_{p/fl}$ (for Cs and As Fig. 9) is controlled mainly by the specific change in surface area of the serpentine mineral, which is related to the initial grain size of the olivine (Lafay et al., 2012). Thus, both spectroscopic measurements and textural arguments indicate that adsorption remains the predominant mechanism for their sequestration (except for Sb as Sb(III) and Sb0). This mechanism is coherent with previous spectroscopic results obtained on As-sorbed at the surface of Mg-minerals in experiments performed at 25 and 50 °C (Opiso et al., 2010). Moreover, with regard to the previous study, Opiso et al. (2010) indicate that the adsorption of arsenate in brucite, hydrotalcite and serpentine at 50 °C is governed mainly by an inner-sphere complexation with oxides or hydroxides coordinated to magnesium (Pokrovsky and Schott, 2004; Morimoto et al., 2009). The presence of pentoxides in our experimental system is consistent with the oxidation state encountered in open-system alteration under oxic conditions, where they represent the predominant form for As and Sb (Filella et al., 2002b; Onishi and Sandell, 1955). Deciphering for one adsorption mechanism is crucial because it implies that FME can be readily remobilized through later changes in the physicochemical properties of the fluid such as temperature (Seewald and Seyfried, 1990) or serpentine recrystallization (Vils et al., 2011; Schwartz et al., 2013; Rouméjon et al., 2015), something that is inherent to the history of natural hydrothermal systems in the abyssal and subduction environments.

In comparison with serpentinite rocks, which display variable FME concentrations, the composition of natural seawater and hydrothermal vents is fairly homogeneous (discussion above). This suggests that differences in FME sequestration are caused mainly by the heterogeneity of the rock. In view of the extreme heterogeneity of natural serpentine geochemistry, even at the same location (Paulick et al., 2006; Deschamps et al., 2013; Andreani et al., 2014), it is hard to estimate the predominant parameters controlling FME partitioning. For example, a study by Deschamps et al. (2010) reports that differences in terms of trace element abundance in serpentine can be related to magmatic inheritance. Additionally, Benton et al. (2004) report changes in the concentrations and isotopic signature of Li as hydrothermal alteration progresses. This might explain concentration gradients and heterogeneous FME distributions at mineral scale (not only for Cs and As (e.g. for Li and B, (Benton et al., 2004; Pabst et al., 2011) as a consequence of (1) the reaction zone considered, (2) the diversity of fluid networks and (3) the change in porosity during the sea-floor serpentinization sequence (Rouméjon and Cannat, 2014).

4.3.3. Accessory phases and serpentinisation conditions

In this study, we revealed that not only serpentine minerals but also brucite (for As(V)) and accessory microphases (which are rarely discussed in natural serpentinites) may carry a large proportion of FME. The evidence of FME distribution in accessory phases has significant implications for the FME trapped in natural serpentinite. In comparison to serpentine minerals, the stability of accessory phases is more dependent on the pH, T, ligands in solution and redox conditions of the serpentinization reaction. In turn, accessory mineral precipitation will impact the FME budget in solution. Accordingly, the nature of the secondary accessory phases that may control the FME distribution in serpentinite rocks may differ from that precipitated in the investigated experimental study (at high FME concentrations in the starting solution). Consequently, the mineral-fluid partitioning of trace element will change. Particularly, the results of the present study reveal that redox conditions may play a crucial role in the sequestration mechanism and uptake of redox-sensitive FME.

In their oxidized form, Sb(V) and As(V) are more mobile and appear mainly adsorbed at the surface of serpentine (and brucite for As). With Sb reduction (into Sb (III) and Sb(0)), there is a change of the sequestration mechanism and its subsequent partitioning into secondary phases (Fig. 10). While As(V) reduction into As(III) was not achieved in the experimental conditions, it is expected that As reduction may also occur in natural hydrothermal systems and then modify the sorption mechanism. In the investigated conditions, we show that it is not serpentine

but brucite that has the highest As partitioning coefficient. This result is consistent with previous observations that shown that brucite is an efficient agent for removing As from fluids (Bochkarev et al., 2010). This experimental result indicates that As may be particularly trapped in natural serpentinite that contained brucite and formed rather after olivine rich peridotite alteration (Moody, 1976), at low temperature (Hyndman and Peacock, 2003) and/or high pH (Lafay et al., 2012).

In natural serpentinite, reduction of redox sensible elements can occur as a concomitant result of Fe oxidation (and water reduction). Changes in redox conditions during progressive serpentinization are expected in rock-dominated ultramafic systems (e.g. Klein et al., 2009; Plümper et al., 2014) occurs at olivine grain boundary during low water–rock incipient serpentinization (Klein and Bach, 2009). This reduction that accompanied serpentinisation reaction (and Fe-oxidation into Fe(III) in serpentine mineral, (magnetite or grossular) lead locally to reduction of redox sensitive elements. It is known that serpentinization reaction in high pH and low fO_2 geochemical environments favors the precipitation of native metals and alloys (Frost, 1985; Klein and Bach, 2009). For example, Plümper et al. (2014) reported the precipitation of awaruite (Ni_2Fe to Ni_3Fe) in the vicinity of veins containing an assemblage of grossular, serpentine, and brucite.

In the alkaline system, fast conversion of olivine to serpentine (with subsequent Fe oxidation) may locally generate sufficient reducing conditions for Sb valence state change and Ni-rich phases precipitation (Wilson et al., 1969; Eckstrand, 1975; Sleep et al., 2004). The most reducing conditions occur for more advanced reaction in the core of former olivine as a consequence of both Fe progressive oxidation and decreasing of fluid availability. The lower solubility of the reduced form of the FME then enhanced their (co)-precipitation. In our study, the high Sb concentrations in solution have clearly favored the precipitation of Sb-rich phases that could correspond to valentinite (Sb_2O_3), breithauptite (NiSb) or nisbite ($NiSb_2$). Based on natural observations, the Sb(III)-rich mineral in our systems could be valentinite (Brookins, 1986; Vink, 1996; Filella et al., 2002a). Such Sb–Ni rich accessory microphases might be specific of the experimental conditions. In natural systems with lower Sb concentrations, Sb will probably be sorbed or precipitated in other oxy-hydroxides and/or sulfides.

To our knowledge, there are no data on the FME distribution in accessory minerals of serpentinites that are commonly too small for such investigations. In many geological contexts, (Onishi and Sandell, 1955; Hannington et al., 1991; Hattori et al., 2005), As and Sb are commonly associated with sulfides, oxides and alloys in a reduced or native form (Wood, 1989; Mosselmans et al., 2000; Filella et al., 2002a; Hattori et al., 2005). In our system, where the activity of sulfide remains limited and no sulfide precipitates, As and Sb appears to be adsorbed on serpentine minerals or precipitated as oxy-hydroxide phases (and/or alloys). This may be different in natural systems, since serpentinites can contain up to 1 wt.% of sulfur in natural hydrothermal system (Delacour et al., 2008a,b; Alt et al., 2012, 2013). Herein, sulfide minerals may be a sink for Sb and As trapping in natural systems in addition to (hydro)oxides under reducing conditions (Wood, 1989; Mosselmans et al., 2000; Filella et al., 2002a; Hattori et al., 2005).

5. CONCLUDING COMMENTS

In the present experimental contribution, accurate mineralogical product characterization provides new results concerning the sequestration of Sb, As, and Cs during olivine serpentinization at 200 °C (Psat) in highly alkaline conditions. Arsenic, Cs and Sb are shown to behave differently throughout serpentinization and several conclusions have been drawn.

I. FME partitioning is dominated by an adsorption mechanism. XAS measurements indicate that, in alkaline conditions, neither As(V) nor Sb(V) are structurally incorporated in serpentine.
II. Estimates for the solid/fluid distribution coefficient after the reaction is complete are 3.8–8.6 and 1.5–1.8 for As and Cs respectively; this concerns serpentine and brucite and the lower values are for the largest initial grain size. The value is much higher in the case of Sb, especially Sb(V) sorbed at the surface of serpentine (up to 65).
III. Antimony speciation and related sequestration mechanisms radically change in response to original Fe(II) oxidation and related modifications in redox conditions. First, Sb(V) is adsorbed by serpentine. Then the reduction of Sb(V) implies remobilization and precipitation of Sb in Sb(III) and possibly Sb(0) as Sb–Ni-accessory phases. The sequestration mechanism (adsorption/precipitation, nature of microphases) remains to be addressed in natural systems with lower Sb concentrations in solution and where sulfides can precipitate.
IV. Arsenic sequestration is controlled by adsorption in serpentine and even more in brucite. In the conditions investigated, As seems to be less redox-sensitive than Sb and the conditions for the reduction of As(V) into As(III) are not reached. Here, arsenate sequestration mechanism remains the same throughout the serpentinization reaction.
V. FME partitioning appears to depend on the initial olivine grain size and subsequent reaction kinetics and/or textural properties of the particles produced. This indicates that FME sequestration is possibly dependent on the fluid flux at the reaction surface (i.e. the ease with which the fluid reaches olivine during serpentinization).

These observations constitute sources of reflection for understanding FME partitioning by serpentine and accessory phases in experimental and natural systems. When possible, a coupled characterization of the in-situ Fe oxidation state and FME distribution, oxidation state and atomic environment will provide a better understanding of element sequestration in serpentinized rock.

ACKNOWLEDGEMENTS

The authors are grateful to the French National Centre for Scientific Research (CNRS) and Joseph Fourier University (UJF) in Grenoble for providing financial support. Alteration reaction and trace element analyses have been possible thanks to equipment and protocols funded by the ANR-MONA-12-JS06-0001-01 project. They also wish to thank N. Findling, V. Batannova, C. Chauvel and F. Toche for their help concerning X-ray diffraction, microprobe, ICP-MS and TGA measurements respectively and concerns about data treatment. Finally, we wish to thank J. Kodolányi and an anonymous reviewer for their critical review comments and W. Bach for editorial work that significantly improved the manuscript.

REFERENCES

Agranier A., Lee C.-T. A., Li Z.-X. A. and Leeman W. P. (2007) Fluid-mobile element budgets in serpentinized oceanic lithospheric mantle: Insights from B, As, Li, Pb, PGEs and Os isotopes in the Feather River Ophiolite, California. *Chem. Geol.* **245**, 230–241.

Allen D. E. and Seyfried W. E. (2003) Compositional controls on vent fluids from ultramafic-hosted hydrothermal systems at mid-ocean ridges: an experimental study at 400 °C, 500 bars. *Geochim. Cosmochim. Acta* **67**, 1531–1542.

Allen D. E. and Seyfried W. (2004) Serpentinization and heat generation: constraints from Lost City and Rainbow hydrothermal systems. *Geochim. Cosmochim. Acta* **68**, 1347–1354.

Alt J. C., Shanks W., Crispini L., Gaggero L., Schwarzenbach E. M., Früh-Green G. L. and Bernasconi S. M. (2012) Uptake of carbon and sulfur during seafloor serpentinization and the effects of subduction metamorphism in Ligurian peridotites. *Chem. Geol.* **322**, 268–277.

Alt J. C., Schwarzenbach E. M., Früh-Green G. L., Shanks W. C., Bernasconi S. M., Garrido C. J., Crispini L., Gaggero L., Padrón-Navarta J. A. and Marchesi C. (2013) The role of serpentinites in cycling of carbon and sulfur: seafloor serpentinization and subduction metamorphism. *Lithos* **178**, 40–54.

Andreani M., Muñoz M., Marcaillou C. and Delacour A. (2013) μXANES study of iron redox state in serpentine during oceanic serpentinization. *Lithos*.

Andreani M., Escartin J., Delacour A., Ildefonse B., Godard M., Dyment J., Fallick A. E. and Fouquet Y. (2014) Tectonic structure, lithology, and hydrothermal signature of the Rainbow massif (Mid-Atlantic Ridge 36° 14′ N). *Geochem. Geophys. Geosyst.* **15**, 3543–3571.

Bach W., Paulick H., Garrido C. J., Ildefonse B., Meurer W. P. and Humphris S. E. (2006) Unraveling the sequence of serpentinization reactions: petrography, mineral chemistry, and petrophysics of serpentinites from MAR 15 N (ODP Leg 209, Site 1274). *Geophys. Res. Lett.* **33**.

Ballhaus C. (1993) Redox states of lithospheric and asthenospheric upper mantle. *Contrib. Mineral. Petrol.* **114**, 331–348.

Benton L. D., Ryan J. G. and Savov I. P. (2004) Lithium abundance and isotope systematics of forearc serpentinites, Conical Seamount, Mariana forearc: Insights into the mechanics of slab-mantle exchange during subduction. *Geochem. Geophys. Geosyst.* **5**.

Blaauw C., Stroink G., Leiper W. and Zentilli M. (1979) Crystal-field properties of Fe in brucite Mg (OH) 2. *Phys. Status Solidi B* **92**, 639–643.

Bochkarev G., Pushkareva G. and Kovalenko K. (2010) Natural sorbent and catalyst to remove arsenic from natural and waste waters. *J. Min. Sci.* **46**, 197–202.

Bonatti E., Lawrence J. R. and Morandi N. (1984) Serpentinization of oceanic peridotites: temperature dependence of mineralogy and boron content. *Earth Planet. Sci. Lett.* **70**, 88–94.

Brookins D. G. (1986) Geochemical behavior of antimony, arsenic, cadmium and thallium: Eh-pH diagrams for 25 °C, 1-bar pressure. *Chem. Geol.* **54**, 271–278.

Carlson R. L. (2001) The abundance of ultramafic rocks in Atlantic Ocean crust. *Geophys. J. Int.* **144**, 37–48.

Charlou J., Donval J., Fouquet Y., Jean-Baptiste P. and Holm N. (2002) Geochemistry of high H_2 and CH_4 vent fluids issuing from ultramafic rocks at the Rainbow hydrothermal field (36° 14′ N, MAR). *Chem. Geol.* **191**, 345–359.

Chauvel C., Bureau S. and Poggi C. (2011) Comprehensive chemical and isotopic analyses of basalt and sediment reference materials. *Geostand. Geoanal. Res.* **35**, 125–143.

Cook N. J. (1996) Mineralogy of the sulphide deposits at Sulitjelma, northern Norway. *Ore Geol. Rev.* **11**, 303–338.

Cressey B. A. and Zussman J. (1976) Electron microscopic studies of serpentinites. *Can. Mineral.* **14**, 307–313.

De Coster M., Pollak H. and Amelinckx S. (1963) A study of Mössbauer absorption in iron silicates. *Phys. Status Solidi B* **3**, 283–288.

Delacour A., Früh-Green G. L. and Bernasconi S. M. (2008a) Sulfur mineralogy and geochemistry of serpentinites and gabbros of the Atlantis Massif (IODP Site U1309). *Geochim. Cosmochim. Acta* **72**, 5111–5127.

Delacour A., Früh-Green G. L., Bernasconi S. M. and Kelley D. S. (2008b) Sulfur in peridotites and gabbros at Lost City (30 N, MAR): implications for hydrothermal alteration and microbial activity during serpentinization. *Geochim. Cosmochim. Acta* **72**, 5090–5110.

Delmelle M. and Gerard A. (1964) Mossbauer effect and ionic character of iron atoms in the orgueil and cold bokkeveld meteorites [effet mossbauer et caractere ionique des atomes de fer dans les meteorites orgueil et cold bokkeveld].

Deschamps F., Guillot S., Godard M., Chauvel C., Andreani M. and Hattori K. (2010) In situ characterization of serpentinites from forearc mantle wedges: timing of serpentinization and behavior of fluid-mobile elements in subduction zones. *Chem. Geol.* **269**, 262–277.

Deschamps F., Guillot S., Godard M., Andreani M. and Hattori K. (2011) Serpenttines act as sponges for Fluid-Mobile-Elements in abyssal and subduction zone environments. *Terra Nova* **23**, 171–178.

Deschamps F., Godard M., Guillot S., Chauvel C., Andreani M., Hattori K., Wunder B. and France L. (2012) Behavior of fluid-mobile elements in serpentines from abyssal to subduction environments: examples from Cuba and Dominican Republic. *Chem. Geol.* **312–313**, 93–117.

Deschamps F., Godard M., Guillot S. and Hattori K. (2013) Geochemistry of subduction zone serpentinites: a review. *Lithos* **178**, 96–127.

Douville É., Charlou J.-L., Donval J.-P., Hureau D. and Appriou P. (1999) Le comportement de l'arsenic (As) et de l'antimoine (Sb) dans les fluides provenant de différents systèmes hydrothermaux océaniques. *C.R. Acad. Sci., Ser. IIA-Earth Planet. Sci.* **328**, 97–104.

Douville E., Charlou J., Oelkers E., Bienvenu P., Colon C. J., Donval J., Fouquet Y., Prieur D. and Appriou P. (2002) The rainbow vent fluids (36 14′ N, MAR): the influence of ultramafic rocks and phase separation on trace metal content in Mid-Atlantic Ridge hydrothermal fluids. *Chem. Geol.* **184**, 37–48.

Eckstrand O. (1975) The Dumont serpentinite; a model for control of nickeliferous opaque mineral assemblages by alteration reactions in ultramafic rocks. *Econ. Geol.* **70**, 183–201.

Essozv J. (1965) Aspects of the geochemistry of arsenic and antimony, exemplified by the Skaergaard intrusion.
Evans B. and Trommsdorff V. (1972) Der einfluss des eisens auf die hydratisierung von duniten. *Schweiz. Mineral. Petrogr. Mitt.* **52**, 251–256.
Evans B. W., Hattori K. and Baronnet A. (2013) Serpentinite: what, why, where? *Elements* **9**, 99–106.
Filella M., Belzile N. and Chen Y.-W. (2002a) Antimony in the environment: a review focused on natural waters: II. Relevant solution chemistry. *Earth Sci. Rev.* **59**, 265–285.
Filella M., Belzile N. and Chen Y.-W. (2002b) Antimony in the environment: a review focused on natural waters: I. Occurrence. *Earth Sci. Rev.* **57**, 125–176.
Foustoukos D. I., Savov I. P. and Janecky D. R. (2008) Chemical and isotopic constraints on water/rock interactions at the Lost City hydrothermal field, 30°N Mid-Atlantic Ridge. *Geochim. Cosmochim. Acta* **72**, 5457–5474.
Fritz B., Clement A., Montes-Hernandez G. and Noguera C. (2013) Calcite formation by hydrothermal carbonation of portlandite: complementary insights from experiment and simulation. *CrystEngComm* **15**, 3392–3401.
Frost B. R. (1985) On the stability of sulfides, oxides, and native metals in serpentinite. *J. Petrol.* **26**, 31–63.
Govindaraju K. (1994) 1994 compilation of working values and sample description for 383 geostandards. *Geostand. Newslett.* **18**, 1–158.
Hannington M., Herzig P., Scott S., Thompson G. and Rona P. (1991) Comparative mineralogy and geochemistry of gold-bearing sulfide deposits on the mid-ocean ridges. *Mar. Geol.* **101**, 217–248.
Hattori K. and Guillot S. (2003) Volcanic fronts form as a consequence of serpentinite dehydration in the forearc mantle wedge. *Geology* **31**, 525–528.
Hattori K. and Guillot S. (2007) Geochemical character of serpentinites associated with high- to ultrahigh-pressure metamorphic rocks in the Alps, Cuba, and the Himalayas: recycling of elements in subduction zones. *Geochem. Geophys. Geosyst.* **8**.
Hattori K., Takahashi Y., Guillot S. and Johanson B. (2005) Occurrence of arsenic (V) in forearc mantle serpentinites based on X-ray absorption spectroscopy study. *Geochim. Cosmochim. Acta* **69**, 5585–5596.
Helz G. R., Valerio M. S. and Capps N. E. (2002) Antimony speciation in alkaline sulfide solutions: role of zerovalent sulfur. *Environ. Sci. Technol.* **36**, 943–948.
Hövelmann J., Austrheim H., Beinlich A. and Anne Munz I. (2011) Experimental study of the carbonation of partially serpentinized and weathered peridotites. *Geochim. Cosmochim. Acta* **75**, 6760–6779.
Hyndman R. D. and Peacock S. M. (2003) Serpentinization of the forearc mantle. *Earth Planet. Sci. Lett.* **212**, 417–432.
Iyer K., Jamtveit B., Mathiesen J., Malthe-Sørenssen A. and Feder J. (2008) Reaction-assisted hierarchical fracturing during serpentinization. *Earth Planet. Sci. Lett.* **267**, 503–516.
James R. H., Allen D. E. and Seyfried W. (2003) An experimental study of alteration of oceanic crust and terrigenous sediments at moderate temperatures (51 to 350 C): insights as to chemical processes in near-shore ridge-flank hydrothermal systems. *Geochim. Cosmochim. Acta* **67**, 681–691.
Jochum K. P., Willbold M., Raczek I., Stoll B. and Herwig K. (2005) Chemical Characterisation of the USGS Reference Glasses GSA-1G, GSC-1G, GSD-1G, GSE-1G, BCR-2G, BHVO-2G and BIR-1G Using EPMA, ID-TIMS, ID-ICP-MS and LA-ICP-MS. *Geostand. Geoanal. Res.* **29**, 285–302.
Kelemen P. B. and Hirth G. (2012) Reaction-driven cracking during retrograde metamorphism: olivine hydration and carbonation. *Earth Planet. Sci. Lett.* **345**, 81–89.
Kerrick D. (2002) Serpentinite seduction. *Science* **298**, 1344–1345.
Klein F. and Bach W. (2009) Fe–Ni–Co–O–S phase relations in peridotite–seawater interactions. *J. Petrol.* **50**, 37–59.
Klein F., Bach W., Jöns N., McCollom T., Moskowitz B. and Berquò T. (2009) Iron partitioning and hydrogen generation during serpentinization of abyssal peridotites from 15°N on the Mid-Atlantic Ridge. *Geochim. Cosmochim. Acta* **73**, 6868–6893.
Klein F., Bach W., Humphris S. E., Kahl W.-A., Jöns N., Moskowitz B. and Berquó T. S. (2014) Magnetite in seafloor serpentinite—some like it hot. *Geology* **42**, 135–138.
Kodolanyi J. and Pettke T. (2011) Loss of trace elements from serpentinites during fluid-assisted transformation of chrysotile to antigorite – an example from Guatemala. *Chem. Geol.* **284**, 351–362.
Kodolányi J., Pettke T., Spandler C., Kamber B. S. and Gméling K. (2012) Geochemistry of ocean floor and fore-arc serpentinites: constraints on the ultramafic input to subduction zones. *J. Petrol.* **53**, 235–270.
Lafay R., Montes-Hernandez G., Janots E., Chiriac R., Findling N. and Toche F. (2012) Mineral replacement rate of olivine by chrysotile and brucite under high alkaline conditions. *J. Cryst. Growth* **347**, 62–72.
Lafay R., Deschamps F., Schwartz S., Guillot S., Godard M., Debret B. and Nicollet C. (2013) High-pressure serpentinites, a trap-and-release system controlled by metamorphic conditions: example from the Piedmont zone of the western Alps. *Chem. Geol.* **343**, 38–54.
Lafay R., Montes-Hernandez G., Janots E., Auzende A.-L., Chiriac R., Lemarchand D. and Toche F. (2014) Influence of trace elements on the textural properties of synthetic chrysotile: complementary insights from macroscopic and nanoscopic measurements. *Microporous Mesoporous Mater.* **183**, 81–90.
Lee C.-T. A., Oka M., Luffi P. and Agranier A. (2008) Internal distribution of Li and B in serpentinites from the Feather River Ophiolite, California, based on laser ablation inductively coupled plasma mass spectrometry. *Geochem. Geophys. Geosyst.* **9**, Q12011.
Ludwig K. A., Kelley D. S., Butterfield D. A., Nelson B. K. and Früh-Green G. (2006) Formation and evolution of carbonate chimneys at the Lost City Hydrothermal Field. *Geochim. Cosmochim. Acta* **70**, 3625–3645.
MacKenzie K. and McGavin D. (1994) Thermal and Mössbauer studies of iron-containing hydrous silicates. Part 8. Chrysotile. *Thermochim. Acta* **244**, 205–221.
Macleod G., McKeown C., Hall A. J. and Russell M. J. (1994) Hydrothermal and oceanic pH conditions of possible relevance to the origin of life. *Orig. Life Evol. Biosph.* **24**, 19–41.
Malvoisin B., Brunet F., Carlut J., Rouméjon S. and Cannat M. (2012) Serpentinization of oceanic peridotites: 2. Kinetics and processes of San Carlos olivine hydrothermal alteration. *J. Geophys. Res. Solid Earth 1978–2012* **117**.
McCollom T. M. and Bach W. (2009) Thermodynamic constraints on hydrogen generation during serpentinization of ultramafic rocks. *Geochim. Cosmochim. Acta* **73**, 856–875.
Mével C. (2003) Serpentinization of abyssal peridotites at mid-ocean ridges. *C.R. Geosci.* **335**, 825–852.
Middleton A. P. and Whittaker E. (1976) The structure of povlen-type chrysotile. *Can. Mineral.* **14**, 301–306.
Moody J. B. (1976) Serpentinization: a review. *Lithos* **9**, 125–138.
Morimoto K., Sato T. and Yoneda T. (2009) Complexation reactions of oxyanions on brucite surfaces. *Nendo Kagaku* **48**, 9–17.
Mosselmans J. F. W., Helz G. R., Pattrick R. A., Charnock J. M. and Vaughan D. J. (2000) A study of speciation of Sb in bisulfide solutions by X-ray absorption spectroscopy. *Appl. Geochem.* **15**, 879–889.

Onishi H. and Sandell E. (1955) Geochemistry of arsenic. *Geochim. Cosmochim. Acta* **7**, 1–33.

Opiso E., Sato T., Morimoto K., Asai A., Anraku S., Numako C. and Yoneda T. (2010) Incorporation of arsenic during the formation of Mg-bearing minerals at alkaline condition. *Miner. Eng.* **23**, 230–237.

Pabst S., Zack T., Savov I. P., Ludwig T., Rost D. and Vicenzi E. P. (2011) Evidence for boron incorporation into the serpentine crystal structure. *Am. Mineral.* **96**, 1112–1119.

Paulick H., Bach W., Godard M., De Hoog J. C. M., Suhr G. and Harvey J. (2006) Geochemistry of abyssal peridotites (Mid-Atlantic Ridge, 15°20′N, ODP Leg 209): implications for fluid/rock interaction in slow spreading environments. *Chem. Geol.* **234**, 179–210.

Philippot P., Busigny V., Scambelluri M. and Cartigny P. (2007) Oxygen and nitrogen isotopes as tracers of fluid activities in serpentinites and metasediments during subduction. *Mineral. Petrol.* **91**, 11–24.

Plümper O., Beinlich A., Bach W., Janots E. and Austrheim H. (2014) Garnets within geode-like serpentinite veins: implications for element transport, hydrogen production and life-supporting environment formation. *Geochim. Cosmochim. Acta* **141**, 454–471.

Pokrovsky O. S. and Schott J. (2004) Experimental study of brucite dissolution and precipitation in aqueous solutions: surface speciation and chemical affinity control. *Geochim. Cosmochim. Acta* **68**, 31–45.

Proskurowski G., Lilley M. D., Seewald J. S., Früh-Green G. L., Olson E. J., Lupton J. E., Sylva S. P. and Kelley D. S. (2008) Abiogenic hydrocarbon production at Lost City hydrothermal field. *Science* **319**, 604–607.

Proux O., Biquard X., Lahera E., Menthonnex J., Prat A., Ulrich O., Soldo Y., Trévisson P., Kapoujyan G. and Perroux G. (2005) FAME: a new beamline for X-ray absorption investigations of very-diluted systems of environmental, material and biological interests. *Phys. Scr.* **2005**, 970.

Ravel B. and Newville M. (2005) ATHENA, ARTEMIS, HEPHAESTUS: data analysis for X-ray absorption spectroscopy using IFEFFIT. *J. Synchrotron Radiat.* **12**, 537–541.

Rona P. A. (1984) Hydrothermal mineralization at seafloor spreading centers. *Earth Sci. Rev.* **20**, 1–104.

Rouméjon S. and Cannat M. (2014) Serpentinization of mantle-derived peridotites at mid-ocean ridges: Mesh texture development in the context of tectonic exhumation. *Geochem. Geophys. Geosyst*.

Rouméjon S., Cannat M., Agrinier P., Godard M. and Andreani M. (2015) Serpentinization and Fluid Pathways in Tectonically Exhumed Peridotites from the Southwest Indian Ridge (62–65 E). *J. Petrol*.

Rüpke L. H., Morgan J. P., Hort M. and Connolly J. A. (2004) Serpentine and the subduction zone water cycle. *Earth Planet. Sci. Lett.* **223**, 17–34.

Savov I. P., Ryan J. G., D'Antonio M., Kelley K. and Mattie P. (2005) Geochemistry of serpentinized peridotites from the Mariana Forearc Conical Seamount, ODP Leg 125: Implications for the elemental recycling at subduction zones. *Geochem. Geophys. Geosyst.* **6**.

Scambelluri M. and Philippot P. (2001) Deep fluids in subduction zones. *Lithos* **55**, 213–227.

Scambelluri M., Fiebig J., Malaspina N., Müntener O. and Pettke T. (2004a) Serpentinite subduction: implications for fluid processes and trace-element recycling. *Int. Geol. Rev.* **46**, 595–613.

Scambelluri M., Müntener O., Ottolini L., Pettke T. T. and Vannucci R. (2004b) The fate of B, Cl and Li in the subducted oceanic mantle and in the antigorite breakdown fluids. *Earth Planet. Sci. Lett.* **222**, 217–234.

Schmidt K., Koschinsky A., Garbe-Schönberg D., de Carvalho L. M. and Seifert R. (2007) Geochemistry of hydrothermal fluids from the ultramafic-hosted Logatchev hydrothermal field, 15°N on the Mid-Atlantic Ridge: temporal and spatial investigation. *Chem. Geol.* **242**, 1–21.

Schmidt M. W. and Poli S. (1998) Experimentally based water budgets for dehydrating slabs and consequences for arc magma generation. *Earth Planet. Sci. Lett.* **163**, 361–379.

Schwartz S., Guillot S., Reynard B., Lafay R., Debret B., Nicollet C., Lanari P. and Auzende A. L. (2013) Pressure–temperature estimates of the lizardite/antigorite transition in high pressure serpentinites. *Lithos* **178**, 197–210.

Seewald J. S. and Seyfried W. E. (1990) The effect of temperature on metal mobility in subseafloor hydrothermal systems: constraints from basalt alteration experiments. *Earth Planet. Sci. Lett.* **101**, 388–403.

Seyfried, Jr., W. E. and Dibble, Jr., W. E. (1980) Seawater-peridotite interaction at 300 °C and 500 bars: implications for the origin of oceanic serpentinites. *Geochim. Cosmochim. Acta* **44**, 309–321.

Seyfried, Jr., W. E., Foustoukos D. I. and Fu Q. (2007) Redox evolution and mass transfer during serpentinization: an experimental and theoretical study at 200 °C, 500 bar with implications for ultramafic-hosted hydrothermal systems at Mid-Ocean Ridges. *Geochim. Cosmochim. Acta* **71**, 3872–3886.

Shannon R. D. (1976) Revised effective ionic radii and systematic studies of interatomic distances in halides and chalcogenides. *Acta Crystallogr. A* **32**, 751–767.

Sherman D. M., Ragnarsdottir K. V. and Oelkers E. H. (2000) Antimony transport in hydrothermal solutions: an EXAFS study of antimony (V) complexation in alkaline sulfide and sulfide–chloride brines at temperatures from 25 C to 300 C at P sat. *Chem. Geol.* **167**, 161–167.

Sleep N., Meibom A., Fridriksson T., Coleman R. and Bird D. (2004) H2-rich fluids from serpentinization: geochemical and biotic implications. *Proc. Natl. Acad. Sci. U.S.A.* **101**, 12818–12823.

Tatsumi Y. (2005) The subduction factory: how it operates in the evolving Earth. *GSA Today* **15**, 4–10.

Thanabalasingam P. and Pickering W. (1990) Specific sorption of antimony (III) by the hydrous oxides of Mn, Fe, and Al. *Water Air Soil Pollut.* **49**, 175–185.

van Keken P. E., Hacker B. R., Syracuse E. M. and Abers G. A. (2011) Subduction factory: 4. Depth-dependent flux of H_2O from subducting slabs worldwide. *J. Geophys. Res.* **116**, B01401.

Vils F., Pelletier L., Kalt A., Müntener O. and Ludwig T. (2008) The lithium, boron and beryllium content of serpentinized peridotites from ODP Leg 209 (Sites 1272A and 1274A): implications for lithium and boron budgets of oceanic lithosphere. *Geochim. Cosmochim. Acta* **72**, 5475–5504.

Vils F., Tonarini S., Kalt A. and Seitz H.-M. (2009) Boron, lithium and strontium isotopes as tracers of seawater-serpentinite interaction at Mid-Atlantic ridge, ODP Leg 209. *Earth Planet. Sci. Lett.* **286**, 414–425.

Vils F., Müntener O., Kalt A. and Ludwig T. (2011) Implications of the serpentine phase transition on the behaviour of beryllium and lithium–boron of subducted ultramafic rocks. *Geochim. Cosmochim. Acta* **75**, 1249–1271.

Vink B. (1996) Stability relations of antimony and arsenic compounds in the light of revised and extended Eh–pH diagrams. *Chem. Geol.* **130**, 21–30.

Viti C. (2010) Serpentine minerals discrimination by thermal analysis. *Am. Mineral.* **95**, 631–638.

Werner C.-D. and Pilot J. (1997) 26. Data report: Geochemistry and mineral chemistry of ultramafic rocks from the Kane Area (MARK). In *Proc ODP, Sci Results*. pp. 457–470.

Wicks F. and Whittaker E. (1977) Serpentine textures and serpentinization. *Can. Mineral.* **15**, 459–488.

Wilson H., Kilburn L., Graham A. and Ramlal K. (1969) Geochemistry of some Canadian nickeliferous ultrabasic intrusions. *Magmatic Ore Deposits, Econ. Geol. Monogr.* **4**, 294.

Wood S. A. (1989) Raman spectroscopic determination of the speciation of ore metals in hydrothermal solutions: I. Speciation of antimony in alkaline sulfide solutions at 25 C. *Geochim. Cosmochim. Acta* **53**, 237–244.

Wunder B., Deschamps F., Watenphul A., Guillot S., Meixner A., Romer R. and Wirth R. (2010) The effect of chrysotile nanotubes on the serpentine-fluid Li-isotopic fractionation. *Contrib. Miner. Petrol.* **159**, 781–790.

Yang L., Shahrivari Z., Liu P. K., Sahimi M. and Tsotsis T. T. (2005) Removal of trace levels of arsenic and selenium from aqueous solutions by calcined and uncalcined layered double hydroxides (LDH). *Ind. Eng. Chem. Res.* **44**, 6804–6815.

Associate editor: Wolfgang Bach